Microphysical properties and light absorption enhancement of refractory Black carbon aerosols in the central Arctic marine boundary layer: Role of warm airmass intrusions on mixing state

Babu Suja Arun[1], Thomas Müller[1], Mira L. Pöhlker[1,2], Andreas Held[3], Christopher Pöhlker[4], Manuela van Pinxteren[1], Yifan Yang[1], Sabine Lüchtrath[3], Andreas Walbröl[5], Janna E. Rückert[6], Philipp Oehlke[1], Maik Merkel[1], Birgit Wehner[1]

[1]Leibniz Institute for Tropospheric Research, 04318 Leipzig, Germany
[2]Leipzig Institute for Meteorology, University of Leipzig, Leipzig, Germany
[3]Environmental Chemistry and Air Research, Technische Universität Berlin, Berlin, Germany
[4]Max Plank institute for Chemistry, Mainz, Germany
[5]Institute for Geophysics and Meteorology, University of Cologne, Germany
[6]Institute of Environmental Physics, University of Bremen, Bremen, Germany

Correspondence to: Babu Suja Arun (arun.babu@tropos.de)

Abstract:

Refractory black carbon (rBC) aerosol particles strongly influence Arctic atmospheric radiative transfer, making it essential to understand their microphysical properties and mixing state. However, in-situ investigations on microphysical properties and mixing state of rBC particles over the central Arctic marine boundary layer are scarce. To address this gap, we carried out a comprehensive investigation of rBC particles in the central Arctic onboard the RV *Polarstern* during the ATWAICE cruise. Our results revealed pronounced spatial and temporal variability in microphysical properties rBC in the Arctic marine boundary layer, governed by transport pathways and removal mechanisms. Under pristine background conditions, rBC mass concentrations were at their lowest (median ~ 0.4-0.6 ng m^{-3}). Warm airmass intrusions into the Arctic atmosphere were found to bring polluted anthropogenic aerosols into this pristine environment with an eightfold increase in rBC mass concentrations (median ~3.4 ng m^{-3}, rBC_{max} ~74 ng m^{-3}). A dominant influence of biomass-burning emissions from Eurasia during the warm airmass intrusion, which coincided with a shift toward larger rBC cores (~264 nm) and moderate coating thickness. The mass median diameter of rBC cores was found to increase with latitude, from the lowest value (~156 nm) in lower-latitude regions influenced by higher anthropogenic emissions to ~220 nm in the high Arctic, consistent with the persistence of aged aerosols under background conditions. The light absorption enhancement of rBC estimated using core-shell Mie theory remained low during warm -air-mass intrusions (~1-1.2) than under background conditions (~1.1-1.6), underscoring a strong dependence of rBC radiative effects in the central Arctic on source regions and aging/processing during long-range transport. This study highlights the complexity of rBC aging and mixing state in the central Arctic, driven by variable source characteristics and summertime processing conditions and will help to increase the accuracy in representing rBC in climate models.

1. Introduction

The Arctic region is experiencing accelerated warming, a phenomenon known as Arctic Amplification. Over the past four decades, this has led to a nearly fourfold increase in surface air temperatures over the Arctic (Rantanen et al., 2022). Many climatic feedback mechanisms contribute to this process, involving interactions between the atmosphere, cryosphere, biosphere, and ocean. The key contributors to Arctic amplification include the decline in sea ice extent and thickness, changes in surface albedo, meridional atmospheric moisture transport, ocean heat transport, and alterations in cloud characteristics (Woods and Caballero, 2016; Beer et al., 2020; Zhang et al., 2018; Thackeray and Hall, 2019; Wendisch et al., 2022). Although greenhouse gases are the primary driver of global warming, atmospheric aerosol particles significantly impact the Arctic climate by influencing the radiative balance through the scattering and absorption of solar radiation, cloud formation, and deposition processes (Haywood and Boucher, 2000; Schmale et al., 2021). The radiative impact of aerosols varies seasonally in the Arctic, as cloud cover, surface reflectivity, and solar radiation fluctuate throughout the year (Quinn et al., 2008; Flanner, 2013). The Arctic aerosol life cycle is highly seasonal, primarily driven by long-range transport, atmospheric processing, and precipitation scavenging (Tunved et al., 2013). Elevated aerosol loadings were found during the Arctic haze period, when aerosol particles were primarily transported from industrialized regions of Eurasia and North America under stable atmospheric conditions (Stohl, 2006). During summer, Arctic aerosols undergo extensive wet scavenging, while photochemical activity and biogenic emissions stimulate new particle formation (Engvall et al., 2008). Low-level clouds contribute to winter and early spring warming by trapping outgoing longwave radiation; whereas in summer, they exert a cooling effect by reflecting incoming solar energy (Zhao and Garrett, 2015). Light-absorbing aerosols can amplify these effects, raising atmospheric temperatures and potentially dissipating clouds (Sand et al., 2013).

One of the most significant climate-forcing aerosol components in the Arctic is black carbon (BC), which is produced by the incomplete combustion of fossil fuels and biomass (Bond et al., 2013). BC contributes to atmospheric warming mainly through three mechanisms: absorbing solar radiation (direct effect), altering cloud properties (indirect effect), and reducing snow and ice albedo when deposited on these highly reflective surfaces (albedo effect) (Flanner, 2013; Sand et al., 2013; Thakur et al., 2021; Gustafsson et al., 2026). Due to the limited number of local BC sources in the Arctic, the majority of BC is transported from mid-latitude regions (Bozem et al., 2019; Croft et al., 2016; Gogoi et al., 2021; Pernov et al., 2022). BC transport into the Arctic lower troposphere is influenced by synoptic-scale circulation patterns and boundary-layer dynamics, with wet scavenging as the dominant removal mechanism (Garrett et al., 2011; Winiger et al., 2017).

The atmospheric lifetime, radiative impact, and cloud-interaction potential of BC aerosols are critically influenced by their microphysical properties, particularly size and mixing state (Ching et al., 2016; Asmi et al., 2025). Freshly emitted BC is typically hydrophobic and externally mixed. In contrast, during atmospheric transport, it undergoes aging via condensation and coagulation, acquiring coatings of organic and inorganic species that enhance its hygroscopicity and cloud condensation nuclei activity (Nenes et al., 2002; Motos et al., 2019a). This transformation not only alters the light absorption efficiency of BC but also modulates its susceptibility to wet scavenging processes, especially nucleation scavenging within clouds (Matsui, 2016; Motos et al., 2019b). BC aging timescales are governed by atmospheric oxidant levels and precursor vapours, both of which vary seasonally

and regionally (Fierce et al., 2015). In the Arctic summer, despite higher photochemical activity, enhanced low-level cloudiness and fog formation may accelerate wet removal of aged BC, allowing relatively fresh or partially aged particles to dominate. Yet, the extent and rate at which BC becomes internally mixed in the Arctic marine boundary layer remain poorly understood. Understanding these microphysical transformations is essential to reduce uncertainties in Arctic BC radiative forcing, especially as climate models often simplify or misrepresent BC aging and removal processes (Ching et al., 2018).

Recent assessments have highlighted substantial uncertainties in Arctic BC emissions, primarily due to the underrepresentation of key sources such as gas flaring, waste burning, and mobile combustion in emission inventories (Schmale et al., 2018). For example, flaring emissions from northern Russia may contribute up to 66% of Arctic BC; however, isotope analyses suggest that this estimate may be too high due to errors in emission factors and spatial distribution (Winiger et al., 2017). Emission inventories vary by up to a factor of three (AMAP, 2015; Schmale et al., 2018), further compounding modelling uncertainties. In addition to emission uncertainties, the transformation of BC through atmospheric aging remains poorly constrained in Arctic conditions. This is particularly relevant in the Arctic MBL, where low temperatures and limited precursor gas concentrations slow BC aging (Fierce et al., 2016), and where summer fog and low-level cloudiness can enhance wet scavenging. Consequently, understanding how BC evolves microphysically, especially how it becomes internally mixed and activates as cloud condensation nuclei, remains a major knowledge gap. These microphysical changes critically influence the radiative efficiency of BC, its atmospheric lifetime, and its eventual deposition.

Despite advances in understanding Arctic aerosols, significant uncertainties remain in understanding BC aerosols and their climatic impacts, particularly regarding their interactions with clouds, transport pathways, and deposition processes, due to limited knowledge of the microphysical properties of BC. There exist long-term ground-based BC measurements from a network of Arctic observatories (e.g., Zeppelin, Ny-Ålesund, Pallas, Barrow, Alert, Tiksi, etc.) (Sharma et al., 2006; Eleftheriadis et al., 2009; Schmeisser et al. 2018; Gogoi et al. 2021), and in recent years numerous aerosol observations have also been made over the Arctic using ground-based stations, aircraft campaigns and shipborne platforms (Raatikainen et al., 2015; Schulz et al., 2019; Park et al., 2020; Jurányi et al., ~~2022,~~ 2023; Zanatta et al., 2023; Heutte et al, 2023; Zieger et al. 2023). However, even now, the detailed understanding of the microphysical properties of refractory BC (rBC) particles remains scarce, especially in the central Arctic marine boundary layer (MBL). With this in mind, we have conducted the aerosol observations onboard RV *Polarstern* (PS131) in the central Arctic during summer 2022 to understand the microphysical properties and mixing state of rBC particles in the central Arctic MBL. This study investigates the rBC loading, its size distribution, mixing state, and light-absorption ~~enhancement, as well as the sources of rBC in~~enhancement in the central Arctic MBL, with a particular focus on the role of warm airmass intrusions in modulating the microphysical properties of rBC.

2. Experimental details

2.1 Study region and general meteorological conditions

Ambient atmospheric aerosol measurements were conducted over the Arctic Ocean aboard the icebreaker RV *Polarstern* (PS131), operated by Alfred Wegener Institute, Germany. The expedition PS131 named **AT**lantic

WAter pathways to the **ICE** in the Nansen basin and Fram Strait (ATWAICE) to the central Arctic, was carried out during the summer period (28th June to 17th August, 2022), during which aerosol measurements were conducted from 29th June to 12th August. The ship track during the campaign is shown in Figure 1. The cruise covered the Arctic Ocean (including both the North Sea and the Greenland Sea) and the remote north-western Greenland Sea. *Polarstern* crossed the Arctic Circle during the night of 2nd July and proceeded towards the eastern Fram Strait, where it navigated between 5th and 10th July through the warm, saline waters of the west Spitsbergen current. By 11th July, *Polarstern* reached the continental slope north of Svalbard, continuing northwest into denser ice on 12th July. On 22nd July, *Polarstern* travelled northwest to the Gakkel ridge, reaching the expedition's northernmost point on 25th July. The southward transit towards the Fram Strait began on 2nd August. ~~By 8th August, *Polarstern* arrived at Scoresby Sund, Greenland.~~ More details about ATWAICE cruise and research area are provided in Kanzow et al. (2023).

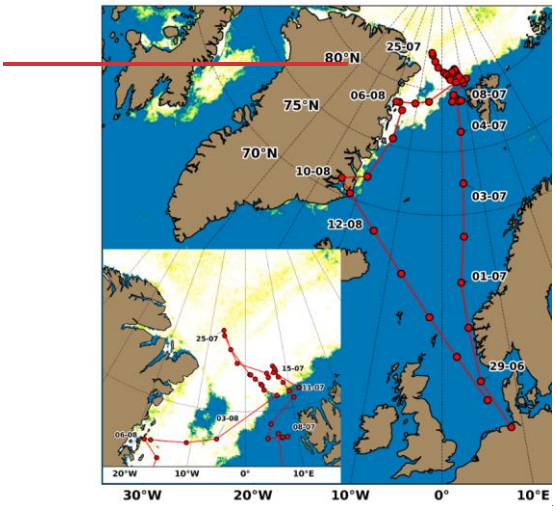

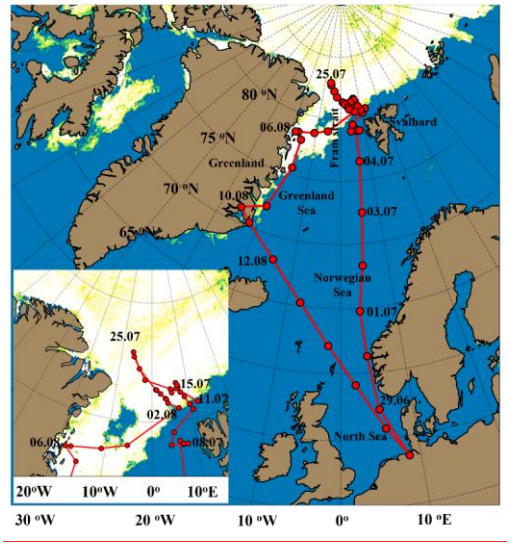

125 **Figure 1:** Ship track of RV *Polarstern* during the ATWAiCE cruise from 28 June to 17 August 2022. The red line indicates the cruise trajectory, with red circle symbols marking the ship's position at local noon each day. The inset shows a zoomed-in view of the northernmost cruise tracks. Background colour indicates Sea ice concentration (MODIS-AMSR2; Ludwig et al., 2020).

Figure S1 illustrates the temporal evolution of meteorological parameters measured aboard RV *Polarstern* during
130 the expedition. Wind speeds generally ranged between 4 and 14 m s^{-1} during the observation period, with several transient peaks exceeding 12 m s^{-1}, notably around 7th to 9th July, 16th to 18th July, and 6th to 8th August. At the beginning of the cruise, while the ship was in the sub-Arctic latitudes and the Norwegian Sea, air temperatures were relatively high (~10 °C to 18 °C), accompanied by moderate relative humidity (RH) values (~60-80%). As the vessel advanced northward into the marginal ice zone and eventually the central Arctic, a marked and sustained
135 drop in temperature occurred beginning around 3rd to 5th July, stabilizing around or below 2-5 °C throughout much of mid-to-late July. During this same period, RH increased significantly, frequently exceeding 90%, indicating a colder, more saturated boundary layer consistent with ice-covered or near-ice environments. A notably colder and humid period is observed from approximately 23rd to 30th July, coinciding with the ship's passage through densely packed sea ice. Mid July (around 15th to 20th July) shows an interesting deviation from the preceding trend, marked
140 by temperature increase (up to ~8 °C) and more variable RH, associated with a warm air mass intrusion over the marginal ice zone. Toward the end of the cruise in early August, another warming phase is noted, particularly from 30th July to 3rd August, when the ship transitioned from ice-covered regions to open-ocean conditions. More details regarding the ATWAICE cruise are available elsewhere (Kanzow et al., 2023).

2.2 Measurements of aerosol particles

145 The measurements of aerosol particles were made from the specifically configured aerosol measurement container on the 'Peildeck' of the ship, with the instruments sampling the air from a common aerosol inlet. To minimize the

Formatted: Space Before: 0 pt

influence of ambient moisture, Nafion membrane dryers were integrated into the sampling system, maintaining the relative humidity of the sampled air below 40%. ~~Nafion membrane aerosol driers were installed in the sampling lines to remove excess moisture, limiting the sampling relative humidity to < 40%~~. Measurements of rBC particles were performed using a Single Particle Soot Photometer (SP2, Model: SP2-D; Droplet Measurement Technologies, USA), which operates at 0.12 L min^{-1}. SP2 utilizes the laser-induced incandescence technique to measure rBC properties using an Nd:YAG laser at 1064 nm (Schwarz et al., 2008). The amplitude of the incandescence signal from SP2 is proportional to the rBC mass present in BC-containing particles (Schwarz et al., 2008).~~.~~

The leading-edge-only (LEO) fitting technique is commonly employed to reconstruct the scattering signal from SP2 (Gao et al., 2007; Liu et al., 2014) to understand the mixing state of rBC. The reconstructed signal is compared with Mie model values to derive the size of coated BC particles. In this approach, the particle is assumed to exhibit a concentric core-shell morphology, represented as a sphere with the core having a refractive index of 2.26 - 1.26i and the coating set at 1.5 + 0i (Moteki et al., 2010). The BC core diameter (Dc) is estimated based on an assumed atmospheric BC density of 1.8 g cm^{-3} (Moteki and Kondo, 2010), while the amplitude of the scattering signal provides information about the scattering cross section of the particles, which is used to derive the optical sizing of the particles (Yang et al., 2025). Prior to measurements, the SP2 was calibrated using Aquadag® black carbon standards, with a correction factor of 0.75 applied to account for differences from ambient BC (Baumgardner et al., 2012; Laborde et al., 2012; Yang et al., 2025). The coating thickness of BC-containing particles is inferred by comparing the optical diameter (D_p) and the Dc.

The absolute coating thickness (CT) is estimated as,

$$CT = (D_p - D_c)/2$$

The mass median diameter (MMD) is determined by fitting BC core size distributions to a monomodal log-normal distribution function (Liu et al., 2019).

To understand the size-resolved coating thickness of rBC particles during the study period, the rBC particles were classified into an i x j grid with i bins for rBC core diameter and j bins for coating thickness. The total volume of rBC containing particles at each grid point is estimated as (Yang et al. 2025),

~~$Volume_{grid\ (i,j)} = \frac{\pi}{6} D^3_{p(i,j)} N_{i,j} = \frac{\pi}{6} (D_{c,i} + 2\ x\ CT_j)^3\ N_{i,j}$~~

$$Volume_{grid\ (i,j)} = \frac{\pi}{6} D^3_{p(i,j)} N_{i,j} = \frac{\pi}{6} (D_{c,i} + 2 \times CT_j)^3\ N_{i,j}$$

where Dp represents the diameter of the rBC containing particle and N indicates the total number of rBC particles.

In this study, the rBC mass concentration was corrected for the missing fraction of rBC (6 ± 4 %) due to the detection limit of SP2. More detailed information regarding SP2, data interpretation procedures, uncertainties, and caveats is available elsewhere (~~Liu et al., 2014;~~ Moteki and Kondo 2010; Yang et al., 2025).

Formatted: Font: (Default) Times New Roman, Not

Formatted: Font: English (United States)

To quantify the impacts of rBC particles in the Arctic, we calculated the absorption enhancement factor (E_{abs}) and mass absorption cross-section (MAC) of rBC particles using Mie theory, constrained by in situ single-particle measurements obtained with SP2 (Yang, 2024). The individual coating thickness was derived assuming a concentric core-shell geometry. To estimate absorption properties, we assumed that each rBC particle can be modelled as a homogeneous spherical core with a concentric, non-absorbing coating (e.g., sulfate or organics). The complex refractive index for the rBC core was set to 1.95 + 0.96i, consistent with literature values for soot, while the coating refractive index was taken as 1.53 + 0i (Moteki et al., 2023; Schnaiter et al., 2005; Zhang et al., 2018). We used a Mie scattering code based on the core-shell solution of Bohren and Huffman (1998) to compute the absorption cross-section of each size bin, both for coated ($C_{abs,coated}$) and bare ($C_{abs,bare}$) rBC particles.

The absorption enhancement factor was then calculated as:

$$E_{abs} = \frac{C_{abs,coated}}{C_{abs,core}}$$

This reflects the increase in light absorption caused by the lensing effect of the non-absorbing coating.

In parallel, the mass absorption cross-section (MAC) was derived using,

$$MAC = \frac{C_{abs}}{M_{rBC}},$$

where M_{rBC} is the mass of the rBC core in each size bin. The MAC values were computed for both bare and coated particles, providing insight into how mixing modifies the specific absorption capacity of rBC under different atmospheric conditions. This enabled direct comparison across regimes with differing aerosol source histories, atmospheric aging states, and mixing conditions.

The light absorption enhancement (E_{abs}) estimated here is using an idealized spherical, concentric core-shell representation (Mie theory based). It should be noted that the real atmospheric BC commonly exhibits complex/fractal morphology and heterogeneous mixing/coating structures, for which core-shell Mie representations can overestimate E_{abs} values that differ from morphology resolved calculations and observations (e.g., Adachi et al., 2010; Ueda et al., 2016; Fierce et al., 2020; Wang et al., 2021; Zhang et al. 2026).

The measurements of equivalent black carbon (eBC) were performed using a multi-angle absorption photometer (MAAP), which measures transmitted and backscattered light from a particle-loaded filter (Petzold and Schönlinner, 2004). Although the MAAP directly measures the absorption coefficient, the results were converted to eBC mass concentration using a predefined mass absorption cross section. In general, eBC measurements were reported at a wavelength of 637 nm, following the recommendations of Müller et al. (2011). A correction factor of 1.05 was applied to account for systematic biases in the retrieval of eBC concentrations. Measurements of light-scattering coefficients were performed using an integrated Nephelometer (Aurora Ecotech 4000). More details regarding this instrument are available elsewhere (Müller et al., 2011).

The aerosol light scattering coefficient was measured using an integrating Nephelometer (Ecotech Aurora 4000). It measures the aerosol total scattering (σsca, between 10º and 170º) and back-scattering coefficients (between 90º

Formatted: Subscript

Formatted: Subscript

Formatted: Font: English (United States)

Formatted: Font: English (United Kingdom)

and 170º) at three wavelengths (450, 525, and 635 nm). The nephelometer data was corrected following the methodology described by Müller et al. (2011). The detailed description of the main characteristics and the working principle of the integrating nephelometers can be found in Müller et al. (2011).

Formatted: Font: English (United States)

In addition, aerosol particle sampling was conducted using a high-volume digital aerosol sampler mounted on the rooftop of the aerosol measurement container. After sampling, the samples were stored in aluminium boxes at -20 ºC and transported to TROPOS, Leipzig, for further chemical analysis. To account for potential contamination during handling and transport, field blanks were prepared by loading the sampler at the sampling site without drawing air through the system. Measurements of organic carbon and elemental carbon were made using a Sunset OC-EC analyser following the EUSAAR II TOT protocol (Birch and Cary, 1996). The concentrations of selected inorganic species were determined in filtered aqueous extracts (0.45 µm syringe filters, 50% of the filter extracted in 2 mL ultrapure water) using ion chromatography (ICS3000, Dionex, Sunnyvale, CA, USA), following the methodology described by Müller et al. (2010). Regular instrument calibration and quality control procedures were implemented to ensure the accuracy and reliability of the analytical measurements.

Ship plumes were occasionally detected during the campaign. To ensure that aerosol measurements were not influenced by emissions from the ship's exhaust, the sampling inlet was installed ahead of the ship's engines. Despite this strategic placement, some data points were still affected by ship emissions and had to be filtered out before further analysis to obtain a dataset representing background aerosol concentrations. The following conditions led to data exclusion: Data points were removed when the relative wind direction ranged between 110° and 260°, as this wind pattern could carry exhaust emissions toward the sampling inlet. Measurements taken at wind speeds below 2 ms^{-1} were discarded since weak winds can cause local turbulence, increasing the risk of exhaust contamination. Sharp increases or abrupt fluctuations in total particle number concentration were considered indicative of contamination and were therefore excluded. Any extreme spikes in the incandescence signal from SP2 were removed, as they were likely linked to ship exhaust plumes. For offline aerosol sampling, an automated pollution-avoidance system was used. This system, which continuously monitored relative wind direction, was integrated with the digital sampler to automatically halt the sampling pumps when airflow originated from the sector associated with ship exhaust contamination.

2.3 Thermodynamic measurements of the atmosphere

A Humidity and Temperature PROfiler (HATPRO) microwave radiometer (Rose et al., 2005) was deployed on the Peildeck, adjacent to the aerosol measurement container during the cruise. This instrument continuously measures atmospheric radiances emitted by water vapor, oxygen, and liquid cloud droplets, utilizing seven frequencies between 22 and 31 GHz along a water vapor absorption line and seven additional channels between 51 and 58 GHz within the oxygen absorption complex. With a high temporal resolution of approximately 1 s, HATPRO provides near-continuous monitoring of key atmospheric variables. The primary observational mode involved zenith-pointing measurements, enabling the retrieval of vertically integrated water vapor (IWV), liquid water path (LWP), and vertical profiles of temperature and absolute humidity following established methodologies (e.g., Walbröl et al., 2022). In a shorter observational mode for 15 consecutive minutes each hour, the instrument was observing the surface, and no measurements of the atmosphere were recorded. Additionally, boundary layer

scanning at multiple elevation angles was conducted to enhance temperature profiling within the lower troposphere.

3. Results and discussion

3.1 Latitudinal variability and source signatures of aerosol particles

Figure 2 shows the temporal evolution of the aerosol light scattering coefficient at 525 nm (σ_{sca}), mass concentrations of equivalent black carbon (eBC) and refractory black carbon (rBC) along the cruise track. σ_{sca}, eBC and rBC exhibited pronounced variability during the campaign, with comparatively high values during the initial, lower-latitude part of the transect and substantially lower values over the central Arctic.

The hourly σ_{sca} ranged from 0.1 Mm^{-1} and 66 Mm^{-1}, with approximately 90% of the observations below 25 Mm^{-1}. Higher σ_{sca} values observed during the beginning of the campaign, whereas σsca remained mostly below 10 Mm^{-1} over much of the high Arctic. As the research vessel moved northern latitudes, σ_{sca} generally decreased and remained low over large parts of the central Arctic. This behaviour is consistent with previous summertime observations in the Arctic reporting low aerosol loadings in the central Arctic compared with lower-latitude regions influenced by marine and continental airmasses (Quinn et al., 2002; Tomasi et al., 2007; Schmeisser et al., 2018; Pandolfi et al., 2018; Gogoi et al., 2021; Schmale et al., 2022).

~~provides an overview of the temporal and spatial variability of equivalent BC (eBC), refractory BC (rBC), and aerosol light-scattering coefficients at 525 nm (σ_{sca}) observed along the latitudinal transect of the cruise track. Hourly σ_{sca} varies over a wide range (between 0.1 Mm^{-1} and 66 Mm^{-1}) with ~90% of σ_{sca} < 25 Mm^{-1}. The higher values of σ_{sca} during the beginning of the campaign is mainly associated with the proximity to the anthropogenic sources from the European continent. The σ_{sca} was generally low (<10 Mm^{-1}) in the high Arctic and increasing during transit toward lower latitudes, particularly south of 70°N. Episodic increases observed in σ_{sca} were potentially associated with long-range transported aerosols, biomass burning plumes or local sources such as sea spray aerosol emissions or marine biogenic emissions. As the *Polarstern* traversed northward, σ_{sca} values steadily declined and remained below 5 Mm^{-1} across large parts of the central Arctic region, which is consistent with the typically low aerosol loading in this region during summer (Schmeisser et al., 2018; Pandolfi et al. 2018; Gogoi et al., 2021). Several earlier studies reported the large spread of light scattering coefficient during the Arctic summer period associated with the sea spray aerosols, biogenic emissions, as well as the anthropogenic influx from Europe (Quinn et al., 2002; Tomasi et al., 2007; Schmeisser et al., 2018; Schmale et al., 2022).~~

Formatted: Superscript
Formatted: Subscript
Formatted: Font color: Auto
Formatted: Justified

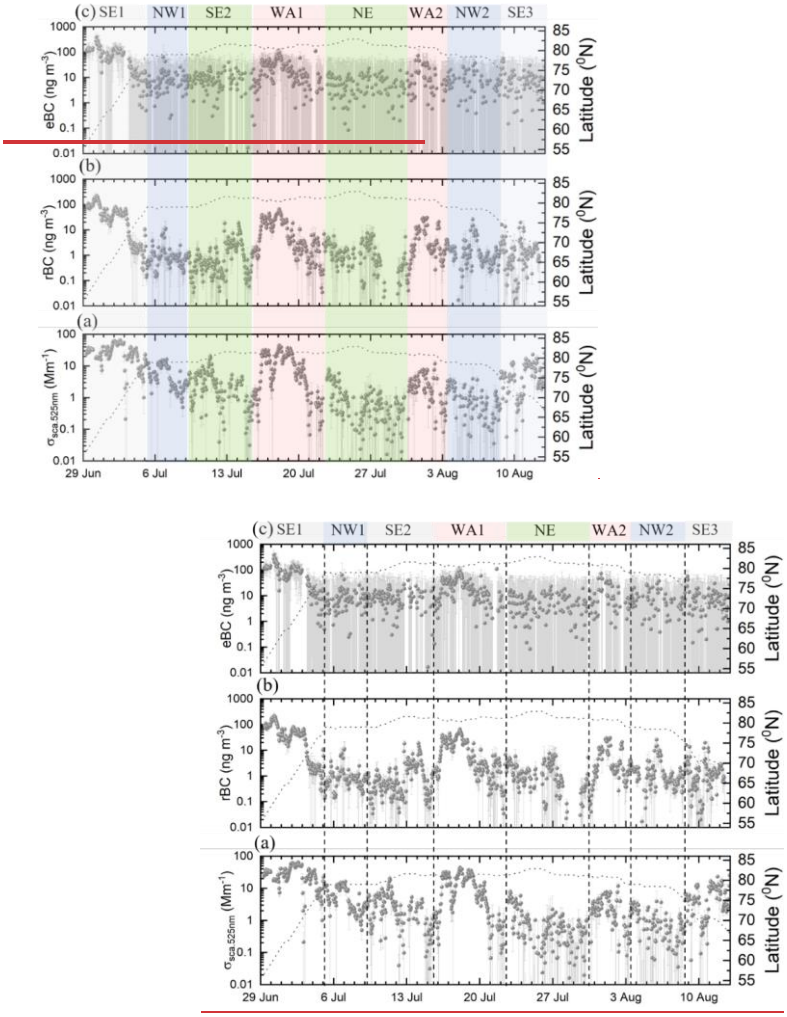

Figure 2: (a) Light scattering coefficient of aerosols measured at wavelength 525 nm using an integrating Nephelometer, (b) Refractory black carbon mass concentration measured using SP2, (c) Equivalent Black carbon mass concentration measured using MAAP. Each subplot is accompanied by a dotted line indicating the corresponding latitude (right y-axis). The vertical grey lines indicate the respective standard deviation for each parameter.

The temporal variability of eBC and rBC broadly followed that of σ_{eca}. During the initial phase of the cruise (29 June- 3 July), when the ship was located at lower latitudes, eBC frequently exceeded 100 ng m^{-3}, with a maximum of 399 ng m^{-3}. North of approximately 70 °N, eBC decreased significantly, and 95% of the subsequent observations remained below 40 ng m^{-3}. The rBC mass concentration (MrBC) exhibited a similar large-scale pattern, with enhanced values during the lower-latitude part of the transect and low concentrations during the

Formatted: Subscript

Formatted: Superscript

observations in the central Arctic. eBC and the mass concentration of rBC (M_{rBC}) also showed significant temporal variability, particularly during the beginning of the cruise (29th June to 3rd July), when the ship was positioned at comparatively lower latitudes. During this period, eBC frequently exceeded 100 ng m^{-3} and even reached 399 ng m^{-3}, indicating the influence of the proximity to the European continental/ship emission sources. Northward of 70°N, starting in early July, eBC concentrations declined markedly, with 95% of the values remaining below 40 ng m^{-3} for the rest of the cruise. This northward decline underscores the relatively clean and isolated nature of the high Arctic atmosphere in summer. The temporal trend of rBC follows that of eBC, with elevated concentrations observed in the sub-Arctic and much lower values in the central Arctic. During the central Arctic transect (approximately 10th to 27th July), both eBC and rBC mass concentrations remained consistently low, indicative of background conditions over sea ice and the open ocean. The measured mass concentrations range aligns well with previously reported values from various Arctic field campaigns (Taketani et al., 2016; Schulz et al., 2019). Nonetheless, episodes of enhanced σ_{sca}, eBC, and rBC were observed from 15th to 22nd July and 30th July to 3rd August, suggesting the transient influence of warm airmass intrusions favourable for enhanced aerosol loadings. This will be discussed in detail in section 3.2.

Although eBC and rBC covaried during the campaign, differences were evident in their absolute magnitudes and short-term variability. These differences likely reflect the distinct measurement principles of the MAAP and SP2, as well as differences in their sensitivity to particle mixing state and aerosol composition (Backman et al., 2017; Asmi et al., 2021, 2025). The correlation between eBC and rBC measured during the study period are provided in the supplementary information (Figure S2). In addition, elemental carbon (EC) derived from filter samples was mostly below the detection limit of the OC-EC analyser throughout the campaign (Figure S3), indicating that filter-based EC measurements had limited applicability under the very low aerosol loadings encountered here. For this reason, the following discussion focuses primarily on SP2-derived rBC, which provides higher sensitivity and time resolution under background Arctic conditions. The observed differences in magnitude and variability of M_{rBC} and eBC, likely reflecting both instrumental differences and variability in aerosol composition (Backman et al 2017; Asmi et al. 2021, 2025). Further, we observed that elemental carbon (EC) concentrations derived from aerosol filter samples were mostly below the detection limit of the OC-EC analyzer throughout the cruise (Figure A2). This highlights the limitations of filter-based techniques in capturing low EC loadings, which are typical of the clean Arctic environment. However, single-particle measurements with the SP2 provide highly sensitive, real-time rBC that is more reliable under such conditions. To better explain the properties of BC, we will focus on rBC in the remaining discussions.

Formatted: Space Before: 12 pt

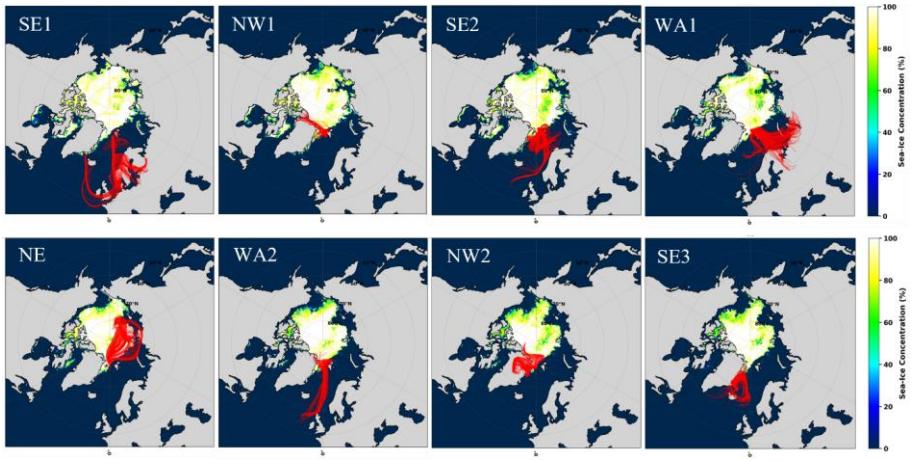

Figure 3: 5-days ~~B~~backward airmass trajectories arriving at the ship position during the campaign segregated into different continuous airmass regimes (SE1- South easterly 1, NW1- North westerly 1, SE2- South easterly 2, WA1- Warm airmass intrusion 1, NE- North easterly, WA2- Warm airmass intrusion 2, NW2- North westerly 2, SE3- South easterly 3) during the study period.

In order to understand the observed variability in the context of airmass transport pathways, 5 days backward airmass trajectories arriving at the ship position (~100 m a.s.l.) were calculated using NOAA Hybrid Single-Particle Lagrangian Integrated Trajectory model (HYSPLIT) (Stein et al., 2015) overlaid on the Arctic Sea ice concentration data from MODIS-AMSR2 (Spreen et al., 2008; Ludwig et al., 2020) during the cruise period. This is further grouped into eight consecutive airmass transport regimes (SE1- South easterly 1, NW1- North westerly 1, SE2- South easterly 2, WA1- Warm airmass intrusion 1, NE- North easterly, WA2 Warm airmass intrusion 2, NW2- North westerly 2, and SE3- South easterly 3; Figure 3). These regimes differ in their dominant transport direction and in the relative time spent over continental, marine, and sea-ice covered surfaces. Figure 4a summarizes the fractional contribution of relative time each airmass regimes spent over these three different surface types. ~~spatio-temporal variabilities in rBC and its sources, airmass trajectory analysis were carried out. Figure 3 shows five days backward airmass trajectories arriving at the ship's position (~100 m a.s.l) estimated using NOAA Hybrid Single-Particle Lagrangian Integrated Trajectory model (HYSPLIT) (Stein et al., 2015) overlaid on the Arctic Sea ice concentration data from MODIS-AMSR2 (Spreen et al., 2008; Ludwig et al., 2020) during the cruise period. These trajectories are grouped into eight consecutive regimes (SE1- South easterly 1, NW1- North westerly 1, SE2- South easterly 2, WAI1- Warm airmass intrusion 1, NE- North easterly, WAI2- Warm airmass intrusion 2, NW2- North westerly 2, SE3- South easterly 3) based on the dominant directions of airmasses arriving at the ship's position. This allows us to identify key transport pathways and surface-type interactions (open ocean, sea ice, continental) relevant to the observed variability in rBC properties during the cruise. Further, we have analysed the residence time of each airmass under distinct surface types, such as continental (indicating airmass transport through continental landmasses), marine (indicating airmass transport through open ocean waters), and sea ice (representing airmass transport over sea ice). Figure 4(a) shows the~~

~~percentage contribution of each of these surface type contributions for the airmasses under consideration in this study~~.

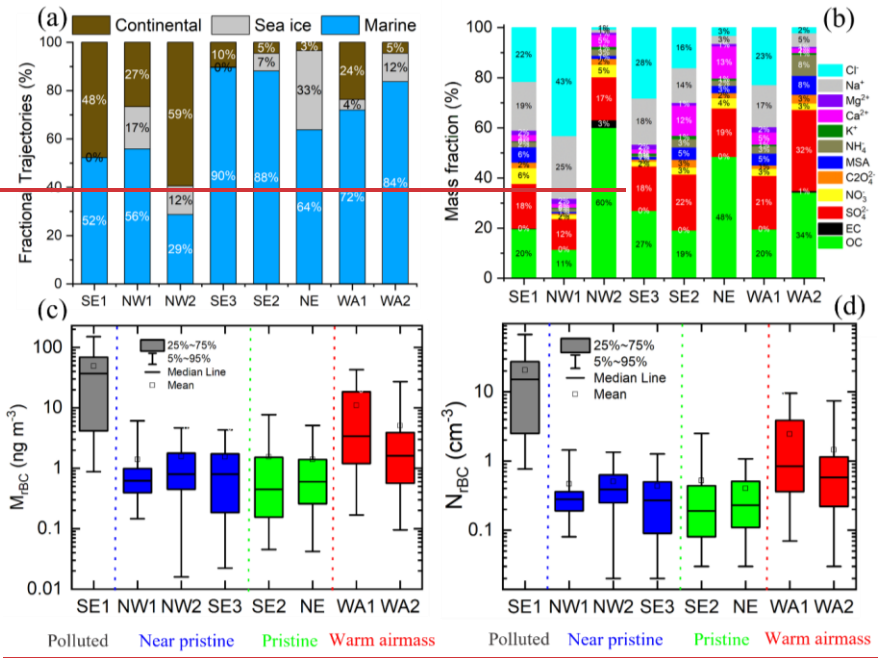

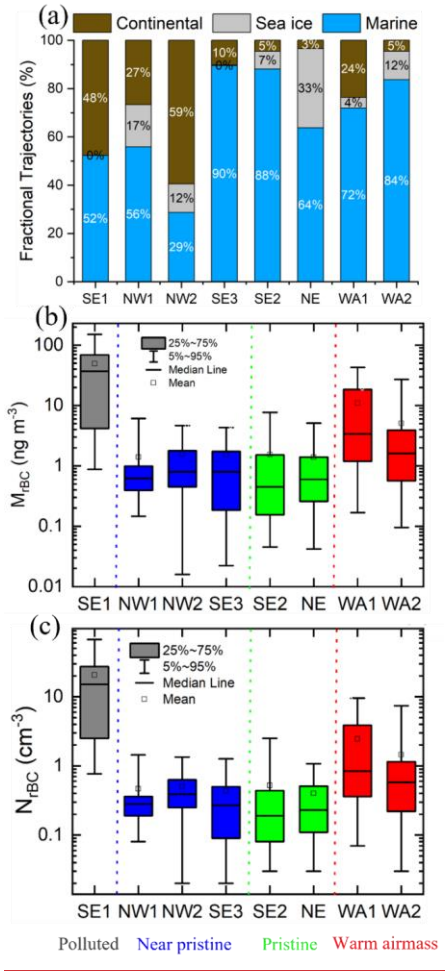

Figure 4: (a) Stacked bar plots representing the fractional contributions of three different surface types traversed by air-masses before arriving at each of the eight designated airmass ~~sectors~~regimes: SE1, NW1, NW2, SE3, SE2, NE, WA1 and WA2. The three categories are: Marine (Blue): Air-masses that predominantly travelled over oceanic regions. Sea Ice (Gray): Air-masses that passed over areas covered by sea ice. Continental (Brown): Air masses influenced by land surfaces. Each bar is segmented and annotated with percentage values indicating the proportion of time the air-masses spent over each surface type before reaching the measurement location, (b) ~~mass fraction of chemical species estimated from offline aerosol measurements~~ , ~~(c)~~ Box and whisker diagram showing the variabilities in mass concentration of refractory BC, (~~d~~c) Box and whisker diagram showing the variabilities in number concentration of rBC particles in each ~~study~~ regime~~s~~.

Among all regimes, SE1 showed the highest rBC concentrations (median ~37 ng m^{-3}; Figure 4c). Airmasses during this period indicate transport from lower-latitude regions with a stronger continental influence than during the

Formatted: Centered

central Arctic regimes, together with substantial residence over marine environments. This regime was also characterized by elevated σ_{sca} (~36 Mm^{-1}) and a comparatively large contribution of Na^+ and Cl^- to the bulk aerosol composition (Figure 5), suggesting the simultaneous presence of combustion related aerosols and sea-salt-containing particles.

~~The analysis revealed distinct spatial heterogeneity in aerosol properties, particularly rBC, linked to distinct airmass origins. The SE1 regime originated mainly over continental Europe, traversing predominantly marine pathways, including the North Atlantic Ocean and the North Sea, with significant anthropogenic influence (Figure 4a). These trajectories passed through industrialized regions and major shipping corridors before entering the Arctic. Correspondingly, SE1 exhibited the highest rBC mass concentrations observed during the campaign (median ~37 ng m^{-3}) (Figure 4c). This points to efficient long-range transport of combustion-derived aerosols and their sustained presence in marine-urban mixed air masses, in addition to direct exposure to aerosol loading. The SE1 regime allows us to compare pristine central Arctic conditions with polluted oceanic conditions. Further, we have noted an enhanced contribution of sea-salt aerosols during this period, as indicated by the dominant contribution of Na^+ and Cl^- (~41%) to the chemical composition (Figure 4b). This could further contribute to the enhanced light scattering coefficient (~36 Mm^{-1}) observed during this period.~~ Interpretation of σ_{sca} variability based solely on PM_{10} bulk chemical composition is inherently qualitative because aerosol light scattering depends strongly on particle size distribution and number concentration, not only on mass fraction. In particular, coarse-mode constituents (e.g., Na^+ and Cl^-) may dominate mass during marine influence, whereas fine-mode sulfate and organic aerosol can contribute significantly to σ_{sca}. Since, our chemical composition of PM_{10} samples represents bulk, 24-h integrated composition across a broad size range, the discussion of it with respect to σ_{sca} is qualitative; scattering depends strongly on particle size distribution and number concentration, and we therefore do not attempt size or component resolved attribution with this. The higher rBC loading observed during SE1 likely reflects the influence of continental outflow and possible shipping emissions, as the measurements were at lower latitudes closer to coastal regions.

In contrast, SE2 and NE were characterized by the lowest rBC concentrations. SE2 was dominated by airmass transport over marine regions (88%) with limited continental influence (~5 %), whereas NE was associated with airmasses travelling largely within the central Arctic, including over sea-ice-covered regions (~ 64 % marine and ~ 33% sea ice). During both regimes, rBC concentrations remained very low, typically below ~0.6 ng m-3, and σ_{sca} was also low (~1 Mm^{-1}), particularly during NE. These observations indicate a weak influence of combustion sources with the generally clean summertime central Arctic boundary layer. The lower σ_{sca} (~1 Mm^{-1}) during NE may additionally reflect a reduced contribution from open-ocean derived aerosol since it traversed significantly through sea ice covered regions.

~~In contrast, the SE2 and SE3 regimes reflect a more remote marine influence (SE2 ~88%, SE3 ~90%). SE2 air parcels mostly traversed through the Barents Sea and the adjacent Arctic Ocean, traveling over open water and marginal ice with minimal continental contact. The rBC concentrations during this regime were among the lowest (~0.45 ng m^{-3}), reflecting limited contributions of anthropogenic sources. SE3 trajectories, although marine-dominated, originated from the northern Atlantic sector, including the Barents and Norwegian Seas. Even though these air masses did not have much contact with continental landmasses, they likely encountered oceanic regions affected by background European outflow or by shipping emissions. As such, rBC levels in SE3 were modest~~

Formatted: Subscript

Formatted: Space Before: 0 pt, After: 0 pt

Formatted: Subscript

Formatted: Subscript

Formatted: Subscript

Formatted: Subscript

Formatted: Subscript

Formatted: Font:

Formatted: Font: English (United States)

Formatted: Font: English (United States)

Formatted: Font: English (United States)

Formatted: Font: English (United States)

Formatted: Font: English (United States)

Formatted: Font: English (United States)

Formatted: Subscript

Formatted: Subscript

~~(mean ~0.8 ng m^{-3}), slightly higher than SE2 but well below SE1, and could represent moderately aged marine aerosols.~~

The NW1, NW2, and SE3 regimes showed intermediate behaviour in rBC properties in comparison with other regimes. The rBC concentrations during these periods were higher than those observed during SE2 and NE, but substantially lower than those during SE1. The airmass transport during this period indicates mixed transport pathways involving different combinations of marine, sea-ice, and more limited continental influence. The low to modest rBC concentrations observed in these regimes suggest either limited source influence, efficient scavenging during transport, or a combination of both. For example, although NW2 exhibited a relatively strong continental influence, the corresponding rBC concentration remained low. This indicates that longer residence time over continental surfaces did not necessarily translate into enhanced rBC concentrations at the receptor site. It is also important to note that the airmasses during this period passed over comparatively remote regions of Greenland, which may have contributed to the observed lower rBC loading. The warm airmass intrusion periods (WA1 and WA2) were associated with episodic enhancements in aerosol properties relative to the surrounding central Arctic background. These events involving additional synoptic-scale influences are discussed separately in the subsequent section.

~~The NE regime, encountered at the northernmost latitudes of the cruise, is significantly influenced by air parcels transported from the central Arctic Ocean over consolidated sea ice conditions (>30% concentration). These air masses were effectively isolated from both continental and lower-latitude marine regions, exhibiting the lowest aerosol concentrations. The rBC levels were consistently minimal (<0.6 ng m^{-3}), and the light scattering coefficients were similarly lower (σ_{sca} ~1 Mm^{-1}). The lower scattering coefficients could also be influenced by the minimal contribution of marine emissions to light scattering, since sea spray emissions are lower than in open ocean waters. These observations reflect the near-pristine Arctic background state, shaped by slow-moving air masses under cold, stable boundary layer conditions with minimal vertical or horizontal mixing.~~

~~NW1 and NW2 showed mixed marine-continental influences. NW1 trajectories originated over northern Greenland, moving over both land and the Greenland Sea before reaching the ship position near the MIZ. The combined land and ocean exposure during this period suggests moderate loadings of aerosol particles from natural sources (e.g., glacial dust, re-suspended particles) and possibly aged Arctic background conditions. The rBC concentrations were similar to the concentrations in the NE regime (median ~0.8 ng m^{-3}). However, NW2 showed an unexpectedly high proportion of continental influence (~59%) based on trajectory surface-type classification, despite having lower rBC concentrations (~0.8 ng m^{-3}). The source region is mostly sea-ice-covered areas north of Greenland and the Fram Strait, suggesting that continental influence here likely came from earlier stages of transport or from the entrainment of aged aerosol layers that had already been scavenged en route. Schmale et al., (2018) noted that interactions among marine, ice-covered, and continental surfaces critically influence aerosol composition and aging in the central Arctic region. Air masses traveling over industrialized zones or biomass-burning regions tend to carry elevated BC and associated pollutants, while those traversing the open ocean or consolidated ice generally yield background or near-pristine conditions. The aging timescale of BC particles is longer in the Arctic due to sparse precursors and limited secondary processing, making the central Arctic MBL particularly susceptible to prolonged periods of low aerosol concentrations, especially in the absence of active~~

~~transport (Schmale et al., 2018). In addition, the lowest rBC concentrations in the central Arctic during the summer period are influenced by efficient scavenging processes due to the thick layers of fog observed during the summer Arctic period.~~

~~Earlier, Taketani et al. (2016) reported pronounced spatial variability in rBC between the North Pacific and Arctic oceans in September, with mass concentrations ranging from 0 to 60 ng m^{-3} and an average of about 1 ng m^{-3}. Schulz et al. (2019) measured rBC in the Canadian Arctic during summer and showed that combustion-derived particles constituted only a minor fraction of the aerosol population. They noted that near-surface rBC concentrations were typically less than 2 ng m^{-3} and that the summer polar dome had little exchange with mid-latitude air masses. Our observed rBC concentrations are lower than those reported by Liu et al. (2015) in the European Arctic during spring, where rBC mass concentrations ranged from 20 to 100 ng m^{-3}, as expected given the general shift toward lower rBC levels from spring to summer.~~ Based on the airmass transport pathways with special emphasis on the relatively dominant residence time over the continental and sea ice surface type, in addition to the rBC concentrations, we have segregated the distinct regimes as, polluted (SE1), near-pristine (NW1, NW2 and SE3), pristine (SE2 and NE) and warm airmass intrusions (WA1 and WA2). The aerosol measurements 29 June to 05 July is marked as 'polluted' whereas the observations NW1, NW2 and SE3 during 05 to 09 July, 03 to 12 August is marked as 'near pristine' and observations during 09 to 15 July and 22 to 30 July is marked as 'pristine'. The measurements during warm airmass intrusion period of 15 to 22 July and 30 July to 03 August is marked as WA1 and WA2. ~~Based on the airmasses histories and the rBC concentrations, we have segregated the distinct regimes as, polluted (SE1), near-pristine (NW1, NW2 and SE3), pristine (SE2 and NE) and warm airmass intrusions (WA1 and WA2).~~

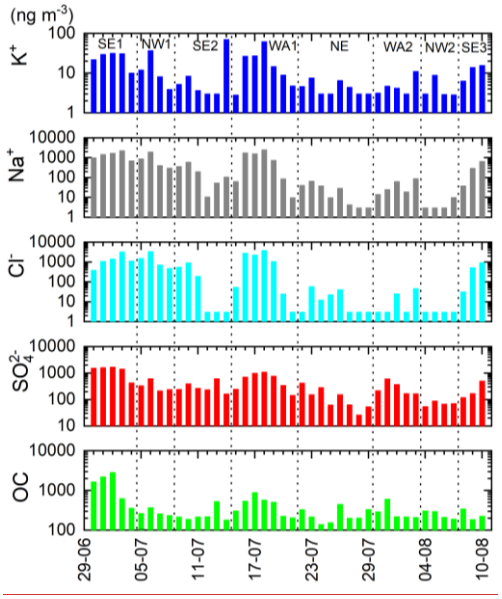

Figure 5: Mass concentration of major chemical species such as OC, SO_4^{2-}, Cl^-, Na^+ and K^+ measured during the study period.

Formatted: Font: English (United States)

Formatted: Subscript

Formatted: Superscript

Formatted: Superscript

Formatted: Superscript

Formatted: Superscript

3.2 Warm airmass intrusions and refractory BC

Two warm airmass intrusion periods were observed during the study period, and both were associated with clear changes in thermodynamic conditions and aerosol properties over the central Arctic. These events interrupted the otherwise lower aerosol conditions that prevailed during much of the campaign and were accompanied by enhanced temperature and rBC concentrations. Previous studies have shown that such synoptic-scale intrusions can efficiently transport heat, moisture, and aerosol from lower latitudes into the Arctic (Mortin et al., 2016; Graham et al., 2017; Henderson et al., 2021; Dekoutsidis et al., 2024).

~~We observed noticeable warm air-mass intrusions into the central Arctic Ocean during the study period, which disrupted the aerosol budget during the expedition. The events caused significant changes in the aerosol properties within a few days, transforming the Arctic from a remote, low-particle environment to conditions more similar to a continental setting in Europe. Recent years have seen an increase in the frequency and duration of these synoptic-scale intrusions, which are brief but intense episodes linked to large-scale blocking (Graham et al., 2017, Mortin et al., 2016; Henderson et al., 2021; Dekoutsidis et al., 2024).~~

The vertical profiles of temperature and absolute humidity retrieved from HATPRO are shown in Figure 6. Between 13and 14 July, an occluded warm front associated with a low-pressure system over the North Atlantic transported warm and moist air. During this period, the temperatures reached up to about 7 °C at an altitude of ~ 600 m. Subsequently, during the WA1 period, two pronounced episodes of warm and humid air were observed between 15and 17 July and between 17 and 19 July. These events were associated with consecutive low-pressure systems south of Svalbard and with strong south-easterly flow transporting warm, moist air towards Svalbard and the adjacent Arctic Ocean (Kanzow et al., 2023). During the second episode, temperatures reached a maximum of 18 °C at ~650 m altitude on 18 July, while integrated water vapour increased to 35 kg m^{-2}. During these events, *Polarstern* was mostly in open water on the lee side of Svalbard. A weaker warm air advection event followed on 19 July, but without a similarly strong increase in humidity. During WA2 (30 July to 3 August), as *Polarstern* began its transit toward the east coast of Greenland into a warm front, warm air masses were observed, with temperatures reaching up to 8 °C at 850 m altitude and integrated water vapor increasing from 14 to 22 kg m^{-2}. Near the surface, temperatures remained close to 0 °C, accompanied by persistent fog. For the following discussion of aerosol properties, the period from 15 to 22 July is defined as WA1, and that from 30 July to 3 August as WA2.

~~The temperature and absolute humidity profiles retrieved from HATPRO are shown in Figure 5. Between 13th and 14th July, an occluded warm front associated with a low-pressure system over the North Atlantic transported warm and moist air. Temperatures reached up to 7° C (at approximately 600 m altitude) during this phase. Subsequently, with the start of regime WA1, two pronounced intrusions of warm and humid air were observed from 15th to 17th July and 17th to 19th July, caused by two consecutive low-pressure systems approaching south of Svalbard. Strong south easterly winds carried significant moisture toward Svalbard and adjacent areas (Kanzow et al., 2023). The second low was especially powerful, with temperatures peaking at 18 °C (at 650 m altitude) on 18 July and a maximum recorded integrated water vapor of 35 kg m^{-2} which is untypically high for polar regions. During these events, *Polarstern* was mostly in open water on the lee side of Svalbard. On 19th July 2022, a third warm air advection event occurred; however, it was weaker than the previous two events and was not accompanied by a~~

Formatted: Not Superscript/ Subscript

Formatted: Superscript

~~significant increase in humidity. A weak high-pressure system led to persistently foggy and cloudy conditions, with some warm air inflow in the two consecutive days. During regime WA2 (30th July to 3rd August), as *Polarstern* began its transit toward the east coast of Greenland into a warm front, warm air masses were observed, with temperatures reaching up to 8 °C at 850 m altitude and integrated water vapor increasing from 14 to 22 kg m-2. Near the surface, temperatures remained close to 0 °C, accompanied by persistent fog. For further discussion of aerosol properties, we considered the warm airmasses from 15th to 22nd July as WA1 and from 30th July to 03rd August as WA2.~~

The two warm airmass regimes differed in their transport history and aerosol characteristics. Based on the backward trajectories shown in Figure 3 and the surface-type influence (Figure 4a), WA1 was associated with transport from the Eurasian sector towards the central Arctic, including substantial passage over the Barents Sea. In contrast, WA2 was characterized mainly by marine inflow from the North Atlantic and Nordic Seas, with comparatively limited continental influence before arrival at the ship position. These differences in transport pathways were reflected in the observed rBC properties and in the PM_{10} chemical composition (Figure 5).

WA1 showed the highest BC enhancement among the central Arctic regimes. During this period, rBC mass concentrations reached up to 74 ng m^{-3}, with a median value of ~3.4 ng m^{-3}, while rBC number concentrations also increased relative to the preceding SE2 period (N_{rBC} ~ 0.84 cm^{-3}, Figure 4b-c). eBC concentrations were similarly enhanced and reached up to 111 ng m^{-3}. These enhanced values indicate that WA1 was associated with episodic transport of pollution into the central Arctic lower troposphere. WA1 is marked by strong continental outflow from Eurasia with strong passage over the Barents Sea towards the central Arctic. This Barents-sector pathway is widely regarded as the most effective corridor for carrying pollutants from northern Eurasian source regions into the Arctic (Stohl et al., 2013). A smaller subset of airmasses was also passing over the Norwegian Sea. In addition, the airmasses associated with WA1 were observed to affect regions known to contribute pollutants to the Arctic, particularly through gas flaring and metallurgical industrial sources (Stohl et al., 2013; Schulz et al., 2019; Dada et al., 2022). The trajectory analysis suggests that the airmasses sampled during WA1 had a stronger influence from lower-latitude source regions than those associated with the clean central Arctic regimes. In addition, the airmasses passed over regions with enhanced fire activity indicated by satellite fire-pixel data (confirmed by MODIS Visible Infrared Imaging Radiometer Suite (VIIRS) satellite data fire-pixel counts, as shown in Figure S4). Along with this, we observed a significant increase in K^+, which supports the predominant role of biomass burning influence during this period over the central Arctic. K^+ has been widely recognized as a good tracer for biomass burning in previous studies (Arun et al., 2019; 2021). The enhanced BC concentrations during WA1 demonstrate the importance of warm airmass intrusions as episodic pathways for transporting biomass burning aerosol into the Arctic marine boundary layer. Similar transport mechanisms have been reported previously for Arctic haze and intrusion events affecting the lower troposphere (Stohl et al., 2013; Schulz et al., 2019; Dada et al., 2022).

~~The two regimes, WA1 and WA2, considered in this study represent warm air mass intrusions from the southeast, with differing source characteristics. The elevated mass concentrations measured during warm air mass intrusions indicate a strong influence of mid-latitude pollution advected into the central Arctic Ocean. WA1 is marked by strong continental outflow from Eurasia with strong passage over the Barents Sea towards the central Arctic. This~~

Formatted: Subscript

Formatted: Superscript

Formatted: Superscript

Formatted: Subscript

Formatted: Superscript

Formatted: Not Highlight

Formatted: Not Highlight

Formatted: Superscript

~~Barents sector pathway is widely regarded as the most effective corridor for carrying pollutants from northern Eurasian source regions into the Arctic (Stohl et al., 2013). A smaller subset of air masses was also passing over the Norwegian Sea. The air masses associated with WA1 were observed to affect regions known to contribute pollutants to the Arctic, particularly through gas flaring and metallurgical industrial sources (Stohl et al., 2013; Schulz et al., 2019; Dada et al., 2022). Further, we have noticed that the trajectories during WA1 passed directly over fire dense regions, as confirmed by MODIS Visible Infrared Imaging Radiometer Suite (VIIRS) satellite data fire pixel counts, as shown in Figure A3. In addition, during WA1, we observed a significant increase in K^+, which supports the predominant role of biomass burning during this period over the central Arctic Ocean. Therefore, we suggest that during WA1, *Polarstern* was strongly impacted by a mix of biomass burning sources and gas flare emissions. As a result, rBC mass concentrations reached as high as 74 ng m^{-3}, and the observed mass concentrations were nearly eightfold (median ~3.4 ng m^{-3}, rBC number concentration ~ 0.84 cm^{-3}, Figure 4c-d), higher than those observed in the preceding period of observations (SE2). This episode demonstrates the ability of warm intrusions to deliver biomass burning aerosols deep into the Arctic marine boundary layer. These observations were aligned with previous findings that underscore the efficiency of synoptic scale transport in delivering anthropogenic and biomass burning aerosols into the Arctic lower troposphere (Dada et al., 2022). The variability in rBC observed within WA1 points to the advection of various anthropogenic air masses and varying vertical mixing, which may be coupled with washout during long range transport and/or secondary processing, as observed, similar to the overall aerosol properties observed during warm airmass intrusions by Dada et al. (2022).~~

In contrast to WA1, WA2 was associated with a lower aerosol loading. During this period, rBC mass concentrations reached up to ~ 35 ng m^{-3}, with a median of ~ 1.6 ng m^{-3}, and the corresponding rBC number concentration ~ 0.58 cm^{-3}. These values are elevated relative to the background regimes but remained clearly lower than those observed during WA1. WA2 was dominated mainly by marine inflow, and the chemical composition showed enhanced SO_4^{2-} and OC contributions relative to WA1. This suggests that WA2 reflected transport of more aged marine and regionally processed aerosol, with a weaker influence from direct combustion sources compared to WA1.

Formatted: Superscript
Formatted: Superscript
Formatted: Superscript
Formatted: Subscript
Formatted: Superscript
Formatted: English (United States)

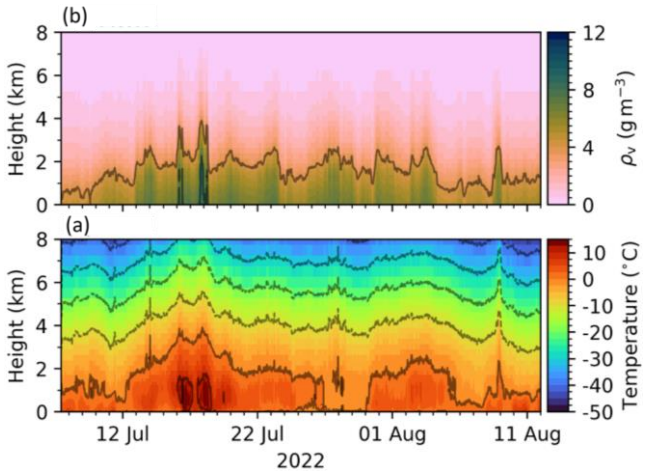

Figure 5~~6~~: (a) HATPRO microwave radiometer retrieval of air temperature (K) vertical profiles, (b) absolute humidity from HATPRO.

Earlier studies have shown that summertime Arctic rBC is generally characterized by very low background concentrations, with occasional enhancements linked to transport. Taketani et al. (2016) reported pronounced spatial variability between the North Pacific and Arctic oceans in September, with rBC mass concentrations ranging from 0 to 60 ng m^{-3} and an average of about 1 ng m^{-3}, while Schulz et al. (2019) observed that combustion particles constituted only a minor fraction of the aerosol population in the Canadian Arctic during summer, with near-surface rBC concentrations typically below 2 ng m^{-3}, reflecting weak exchange between the summer polar dome and mid-latitude airmasses. In the present study, most airmass regimes, including NW 1, NW2, SE 2, SE3, and NE, exhibited similarly low mean rBC concentrations of about 1.4-1.6 ng m^{-3}, with median values of 0.5-0.8 ng m^{-3}, indicating that these conditions represent the clean summertime Arctic background (AMAP, 2015; Zanatta et al., 2023; Jurányi et al., 2023). Our observed rBC concentrations are also lower than those reported by Liu et al. (2015) in the European Arctic during spring, where rBC mass concentrations ranged from 20 to 100 ng m^{-3}, as expected from the seasonal transition from the spring Arctic haze period to the comparatively cleaner summer atmosphere. At the same time, the two warm airmass intrusion cases demonstrate that episodic transport can still substantially perturb this otherwise low-rBC environment. These enhanced values are comparable to or approach those reported at Arctic receptor sites such as Pallas, Finland (26 ng m-3; Raatikainen et al., 2015) and Zeppelin, Svalbard (39 ± 23 ng m^{-3}; Zanatta et al., 2018), but remain far lower than those reported for marine and continental regions outside the Arctic, including the remote Antlantic Ocean(~100 ng m^{-3}) (Pan et al. 2026), south-eastern Arabian Sea (938 ± 293 ng m^{-3}), northern Indian Ocean (546 ± 80 ng m-3), equatorial Indian Ocean (206 ± 114 ng m^{-3}) (Kompalli et al., 2021), Thumba (670 ± 571 ng m^{-3}; Nithin et al., 2026), Mukteshwar in the Himalayas (1000 ± 600 ng m^{-3}; Raatikainen et al., 2017), and Lulang on the Tibetan Plateau (310 ± 550 ng m^{-3}; Wang et al., 2018). ~~The BC concentrations measured under near pristine and pristine conditions fall within the range typically reported for the Arctic summer (AMAP, 2015; Zanatta et al., 2023; Jurányi et al., 2023). In contrast, t~~The markedly enhanced BC levels during WA1 (eBC as high as 111 ng m^{-3}, rBC as high as 74 ng m^{-3}), while clearly elevated relative to background, remain lower than the values observed during warm air-mass intrusions in spring (Dada

Formatted: Superscript

et al., 2022), in subarctic environments, and in near-source high-Arctic sites (Popovicheva et al., 2017). Table 1 summarizes our observed M_{rBC} values in comparison with those reported in previous studies from marine, remote, coastal environments.~~It is also important to note that those studies quantified equivalent BC using an Aethalometer; differences in measurement technique may therefore influence comparisons of absolute BC magnitudes. In contrast, WA2 represents clean marine inflow from the North Atlantic or Norwegian and Greenland seas, moving north through the Fram Strait/western Barents MIZ, with minimal continental (land) influence before arriving at the position of the *Polarstern*. The rBC mass concentration reached as high as 35 ng m^{-3} during this period (median ~1.6 ng m^{-3}, rBC number concentration ~ 0.58 cm^{-3}), which is comparatively lower than WA1, reflecting the influence from aged marine air enriched with enhanced sulfate and OC (Figure 4b).~~

Formatted: Subscript

Formatted: Font: English (United States)

Table 1: rBC mass concentration and mass median diameters reported in this study and the values available from previous studies in the marine, remote and coastal environments.

Location/Region	rBC mass concentration (ng m^{-3})		Mass median diameter (nm)	Reference
	Mean ± SD	Median		
Marine environments				
South easterly 1	48.7 ± 49.8	36.8	156	Present study
North westerly 1	1.4 ± 3	0.6	207	Present study
North westerly 2	1.6 ± 2.5	0.8	217	Present study
South easterly 3	1.6 ± 3	0.8	218	Present study
South easterly 2	1.6 ± 3	0.5	190	Present study
North easterly	1.4 ± 2.7	0.6	227	Present study
Warm airmass intrusion 1	11 ± 14.4	3.4	264	Present study
Warm airmass intrusion 2	5.1 ± 8.3	1.6	220	Present study
Pallas, Finnish Arctic	26		161-231	Raatikainen et al. (2015)
Arctic Ocean	1 ± 1.2		~170	Taketani et al. (2016)
Zeppelin, Arctic	39 ± 23		240	Zanatta et al. (2018)
Alert	22 ± 13		160 - 180	Sharma et al. (2017)
Southern Ocean	0.14			Fossum et al. (2022)
South-eastern Arabian Sea	938 ± 293		190	Kompalli et al. (2021)
Northern Indian Ocean	546 ± 80		200	Kompalli et al. (2021)
Equatorial Indian Ocean	206 ± 114		190	Kompalli et al. (2021)
Remote Antlantic	100		180	Pan et al. (2026)
Remote environments				

Jungfraujoch, Switzerland	13.24	1.4 - 20.5	220-240	Liu et al. (2010)
Lulang, Tibetan Plateau, China	310± 550		160	Wang et al. (2018)
Mukteshwar, the Himalayas, India	1000 ± 600		205	Raatikainen et al. (2017)
North-eastern Qinghai–Tibetan Plateau, China	160 ± 190		187	Wang et al. (2015)
Melpitz	160		140	Yang et al. (2025)
Fukue Island Japan	160 ± 50		200 -220	Shiraiwa et al. (2008)
Catalina Island	40 ± 10		153 - 170	Ko et al. (2020)
Coastal sites				
Thumba	670 ± 571		192	Nithin et al. (2026)
Mace Head	3.31			Fossum et al. (2022)

3.3 Size distribution of refractory BC particles

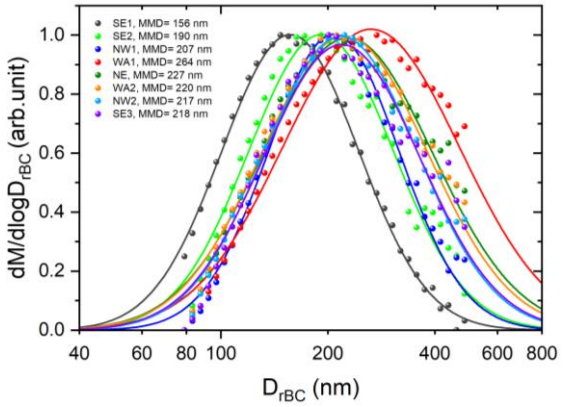

Figure ~~6~~7: Mass size distribution of refractory black carbon particles estimated during the ATWAICE cruise during distinct airmass conditions.

Figure 7 shows the mass size distributions of rBC particles for the different airmass regimes during the cruise. The size distribution of rBC is relevant for interpreting its atmospheric processing and radiative effects, as the light absorption properties of BC depend on core size, while the observed mass median diameter (MMD) can be influenced by source characteristics as well as by aging and removal during transport ~~The light-absorption properties of rBC aerosols are directly related to their size distribution, which is influenced by sources, sinks, and transformation processes during atmospheric long-range transport (Liu et al. 2019). Previous studies have demonstrated that rBC cores emitted from fossil fuel combustion sources typically exhibit smaller MMDs than~~

those from biomass and biofuel burning (Shiraiwa et al., 2007; McMeeking et al., 2010; Liu et al., 2014; Taylor et al., 2014; Kompalli et al., 2020, 2021; Yang et al., 2025). Figure 6 shows the mass size distribution of rBC particles estimated for different airmass regimes during the study period.

The estimated MMD varied substantially across the different transport regimes. During SE1, the estimated the MMD is was ~156 nm, i.e., the lowest among all regimes in this study. This values lies within the range commonly which resembles values typically observedreported for in urbanpolluted environments influenced by dominant fossil fuel emission sourcescombustion, although such comparisons should be interpreted cautiously because the observed size distribution at the receptor site reflects not only source emissions but also atmospheric processing during transport (Laborde et al., 2013; Liu et al., 2019; Kompalli et al., 2020; Lim et al., 2023). As the ship moved away from the lower-latitudes towards the central Arctic, the MMD increased progressively; to ~ 190 nm during NW1, ~207 nm during SE2, and ~ 225 nm during NE. As discussed before, this period was predominantly influenced by European continental outflow, a major source of fossil fuel combustion emissions that generally produce smaller rBC cores. As the ship transitioned to NW1, the MMD gradually increased to ~190 nm, influenced by the changes in airmass characteristics. As the vessel continued towards SE2 in the MIZ, the MMD further increased to ~207 nm, with air masses originating predominantly from the south-eastern oceanic sectors north of Europe. MMD increased further (MMD ~225 nm), as the ship advanced into the higher latitude packed ice conditions. This is associated with air masses predominantly from the northeast, traversing extensively over sea ice. Air masses originating from the northwest (Greenland region) Dduring NW2 and SE3, the MMD remained similarly larger, at ~217 nm and ~218 nm, respectively. resulted in an MMD of ~217 nm. As the ship entered the Greenland zone, the MMD remained similar as NW2 (~218 nm), despite a shift in airmass transport from south-easterly flow. The observed MMDs clearly show an increase in rBC cores across latitudes from Europe to the central Arctic. This increase in MMD suggests a reduced influence from fossil fuel sources and a dominant role for biomass burning emissions in the central Arctic region via long-range atmospheric transport.These observations of MMD indicate a systematic increase in rBC core size from the lower-latitudes towards the central Arctic regimes. However, this gradient should not be interpreted as a unique fingerprint of changing emission sources. In remote regions, rBC size distributions can be modified during transport by size-dependent removal and atmospheric processing, including cloud processing and coagulation (Pan et al., 2026). Therefore, in the absence of independent source-specific tracers and high-resolution chemical composition information, the increase in MMD towards higher latitudes is interpreted here as reflecting the combined effects of distinct sources and atmospheric processing rather than as direct evidence of a transition to a specific source type.

Interestingly, we noticed an A pronounced enhancement in the MMD was observed during the warm airmass intrusion regime WA1, for which the estimated MMD was higher than of rBC particles (~264 260 nm.) during the warm airmass intrusion (WA1). This clearly indicates that biomass burning aerosol particles were transported to elevate the MMD of rBC during this period, as discussed before, with the enhanced rBC contribution heavily associated with intense biomass burning aerosols from Eurasia, in addition to gas flare emission sources. This value is substantially larger than those observed during the background central Arctic regimes and coincided with enhanced rBC mass concentrations during the same period. As discussed in Section 3.2, WA1 was associated with transport from lower-latitude source regions along with the evidence for biomass burning influence. Further, during the warm airmass intrusionIn contrast, during WA2, the MMD of rBC remained close to ~220 nm,

Formatted: Font: English (United Kingdom)

Formatted: Font: English (United Kingdom)

Formatted: Font: English (United Kingdom)

Formatted: Font: English (United Kingdom)

comparable to the values observed during the central Arctic background conditions.~~, similar to typical central Arctic conditions, as discussed earlier. It should be noted that the airmass during WA1 contributed by landmass was ~23%, whereas during WA2 it was only ~6%, with little influence from biomass-burning source regions. This clear distinction in the MMD of rBC particles in the central Arctic indicates that the MMD of rBC particles is primarily dependent on the characteristics of the source region. Relative to background conditions, the intrusion exerted a strong influence on both the rBC mass loading and the microphysical properties of rBC aerosols in this remote Arctic Ocean. This in contradiction with previous studies, which reported that warm airmass intrusions do not affect the microphysical properties of aerosols in the central Arctic (Dada et al., 2022).~~ This difference between WA1 and WA2 further indicates that warm airmass intrusions into the central Arctic do not exert a uniform influence on the microphysical characteristics of rBC; rather, their effect on rBC size distribution depends on the transport pathways and the atmospheric processing within the advected airmass.

~~The~~ Changes in MMD ~~of rBC may change~~ during long-range atmospheric~~distance~~ transport ~~as the particles undergo atmospheric~~can arise from multiple competing ~~-~~ process~~es~~~~ing~~. Size dependent wet removal may preferentially remove ~~L~~larger BC containing particles under some conditions and thereby shift the distribution towards smaller diameters ~~cores are more effectively removed by wet scavenging, which can push the MMD toward smaller sizes because the air mass may encounter clouds and precipitation during transport~~ (Moteki et al., 2012; Schulz et al., 2019). Conversely, ~~However,~~ coagulation and condensational aging may increase the apparent characteristic size of BC containing particles or preferentially preserve larger cores under specific transport conditions ~~may occur as particles age, potentially shifting the distribution toward larger sizes~~ (Tunved et al., 2013~~;~~~~). This indicates that atmospheric processing during transport, in addition to the emission source, shapes the rBC mass-size distribution we observe~~ (Schulz et al., 2019). The observed MMD thus reflects the combined influence of source emissions, removal, and atmospheric processing. This is particularly ~~crucial~~ relevant in the Arctic, where transport pathways, cloud interactions, and scavenging processes jointly control the abundance and properties of BC reaching the central Arctic atmosphere ~~because cloud-driven removal and BC transport into the area can happen simultaneously and support one another~~ (Liu et al., 2011; Schulz et al., 2019). ~~Because of this, the size distribution of rBC alone hardly provides a fingerprint of the primary removal mechanism or the dominant source type.~~

The MMD values ~~Our~~ observed ~~MMD values are~~during this campaign are within the broad range reported previously for Arctic and other remote environments, although substantial variability exists across regions and airmass transport regimes.~~-~~ In the present study, MMD ranged from ~156 nm during SE1 to ~264 nm during WA1, whereas the Arctic background regimes were characterized by MMD around 190-227 nm. These values are comparable to those reported for the Arctic Ocean in summer ~~(higher than those reported for the high Canadian Arctic by Schulz et al. (2019), who found rBC MMDs in the range of 119-134 nm. In addition, our observed MMD values are higher than those observed in summertime measurements over the North Pacific Ocean, the Bering Sea, and the Arctic Ocean, where MMDs varied from 168 to 192 nm (~170 nm;~~ Taketani et al.~~,~~ (2016~~).~~), Pallas in the Finnish Arctic (161-231 nm; ~~R~~aatikainen et al., 2015) , and ~~Earlier, Liu et al. (2015) reported an MMD of ~190 -210 nm during spring during the ACCACIA campaign. Zanatta et al (2018) reported rBC MMD of ~ 240 nm during spring in the~~ Zeppelin during spring~~observatory~~ (Zanatta et al. 2018), but are higher thatn the 119-134 nm reported for the high Canadian Arctic by Schulz et al. (2019). Previous studies from other remote and

Formatted: Font: (Default) Times New Roman, 10 pt

coastal environments similarly show a wide spread, including 140 nm at Melpitz (Yang et al., 2025), 153-170 nm at Catalina Island (Ko et al. 2020), 200-220 nm at Fukue Island (Shiraiwa et al., 2008), and ~192 nm at Thumba (Nithin et al. 2026). These comparisons indicate that the MMD values measured in this study are generally high relative to those reported for other maine/remote/coastal environments.

3.4 Mixing state of refractory BC containing particles

Figure ~~7~~ 8 shows the ~~size~~ size-resolved coating thickness of rBC particles estimated during the study period, along with the ~~volume of rBC particles~~normalized rBC particle volume. The size resolved coating thickness (CT) of rBC particles, along with the number concentration of particles is given in the supplementary Figure ~~A4~~S5. The size resolved CT classification provided a more direct insight into the mixing state of rBC particles in this study.

It is evident that, throughout the study period, two distinct regions of rBC core sizes (below Dc~150 nm and above Dc~150 nm) consistently exhibited relatively higher volume of coated rBC. This suggests that the rBC population during the campaign exhibited pronounced mixing-state heterogeneity. The repeated occurrence of two enhanced-volume domains, one associated with smaller cores and another with larger cores, indicates that non-BC material was distributed unevenly across the rBC population, with some particles remaining weakly processed while others acquired substantial coatings. This particle-to-particle variability is important because the radiative effects of rBC depends not only on the mean coating thickness but also on how the coating is distributed among particles of different core sizes, as emphasized in recent studies (Fierce et al., 2016, 2020; Zeng et al., 2024; Zhai et al., 2022).

The higher contribution from coated larger rBC cores under the northerly and near-pristine regimes likely reflects aged, internally mixed particles that underwent substantial atmospheric processing during long-range transport to the central Arctic. In this study, we found the relatively higher coated volume observed at both smaller and larger cores during SE2 and WA1 points to a broader spread of core-shell combinations, implying a more diverse and complex mixing state under those regimes in the Arctic. Such a pattern suggests that, in addition to aged large-core particles, a greater fraction of smaller rBC cores had also acquired sufficient condensed material to become internally mixed. ~~consistently exhibited high volumes of coated rBC. However, higher volumes of coated rBC in the lower size range (<120 nm) are observed during SE1 and WA1. This shows the capability of warm airmass intrusions to bring higher abundances of coated rBC particles in smaller size ranges to the central Arctic, similar to regions highly influenced by continental anthropogenic exposures.~~ Condensational aging generally enhances coating accumulation more efficiently on smaller BC cores than on larger ones (Seinfeld and Pandis, 2006). The bottom-left region with null values corresponds to smaller rBC particles that show neither positive nor negative coating thickness (CT), due to the detection limitations of the SP2 ~~instrument~~, as reported in several studies (Ko et al., 2020; Yang et al., 2025). This detection limitation restricts the retrieval of coating information from scattered light for smaller rBC particles. As a result, the mixing state ~~of~~ information of a substantial portion of these smaller rBC particles remains unresolved. ~~The average CT estimation may be skewed by the lack of CT details for smaller rBC particles. Only coated rBC particles with rather thick coatings are found for particles smaller than 150 nm, leading to an overestimation of the mean CT.~~This missing fraction of CT results in overestimation of CT when estimating the absolute coating thickness across the entire size range.

Formatted: English (United States)

~~It is interesting to note a higher volume of rBC with core sizes >150 nm, except for SE2 and SE3. It is found that, although these two regions are influenced by southerly airmasses, they are mostly transported over open ocean regions, as evident from Figure 4(a). The lower contribution of continental airmasses (~5%) in comparison with relatively higher contribution of continental airmasses (~10%) could have contributed to relatively higher coated particles to SE3. Further, regions with higher volumes of rBC with core sizes >150 nm are prominent during NW1, NW2 and NE. The difference in the proportion of non-BC material among BC-containing particles of different core sizes can be defined as mixing-state heterogeneity, as previously reported in several studies (Zeng et al., 2024; Zhai et al., 2022). This heterogeneity is critical in understanding the absorption enhancement of coated rBC (Fierce et al., 2016; 2020; Zeng et al., 2024).~~

In order to provide a statistical insight into the mixing state information of rBC particles, the frequency distribution of CT estimated in the 180-300 nm is shown in Figure ~~8~~9. The median CT for the near pristine, pristine and warm airmass conditions during the study ~~varied~~ ranged from from 14nm-18 nm, 9nm-20 nm and 12nm-15 nm respectively. It is found that coating thickness was relatively higher in regions influenced mainly by northerly air mass advections (NE, NW1 and NW2, with CT_{median} ~ 20 nm ~~and~~ , CT_{median} ~ 18 nm, and CT_{median} ~ 18 nm respectively), while the lowest coating thickness is found during SE2 (CT_{median} ~ 9 nm). ~~The lower SE2 coating thickness compared to SE1, despite larger rBC cores, suggests less photochemically processed aerosols or lower availability of condensable materials in this relatively clean, higher-latitude region. Further, the lower coating thickness at SE2 could also be due to higher cloud scavenging during this period, as evidenced by denser fog layers associated with lower visibility (Kanzow et al. 2023) during SE2.~~

In northerly airmass regimes, ~~these~~ air ~~masses~~ likely experienced prolonged atmospheric residence times and active secondary aerosol condensation, leading to more internally mixed, coated rBC particles. Specifically for the northerly airmasses, we observed a higher fractional contribution to the total aerosol mass ~~(Figure 4b)~~ from ~~sulfate (~~SO_4^{2-}, ~18%~~)~~ and ~~organics (~~OC~~,~~ ~48%~~)~~ especially during NE. The prolonged transport through marine and sea ice covered environments (Figure 4a) and the associated extended atmospheric aging of rBC particles during NE could have facilitated the condensation of secondary species onto rBC cores. However, for the NW2, particularly when the ship was located in the Greenland Sea, the contributions from SO_4^{2-} and OC were even higher. These increased fractions of organics and sulfate may have contributed significantly to the observed enhancement in the coating of rBC cores during this period. It is important to note that the NE regime was predominantly influenced by air masses traversing oceanic and sea-ice-covered regions, whereas the NW2 regime was more strongly affected by continental outflow from Greenland. However, ~~because~~ since simultaneous real-time submicron aerosol chemical composition measurements are not available alongside rBC data, we cannot definitively attribute the enhanced coating to these chemical species. Furthermore, the $PM_{1.0}$ chemical composition discussed above reflects bulk aerosol composition integrated over a 24-hour period and across a broad size range, its relationship to SP2-derived submicron rBC coating thickness is qualitative; therefore, sulfate and OC fractions should not be interpreted as quantitative indicators of rBC coating.

~~the fractional contributions shown in Figure 4b are derived from daily $PM_{1.0}$ filter samples, which may introduce biases while interpreting SP2-derived coating thicknesses, as the SP2 specifically measures submicron aerosols~~.

Formatted: Space Before: 0 pt

Formatted: Subscript

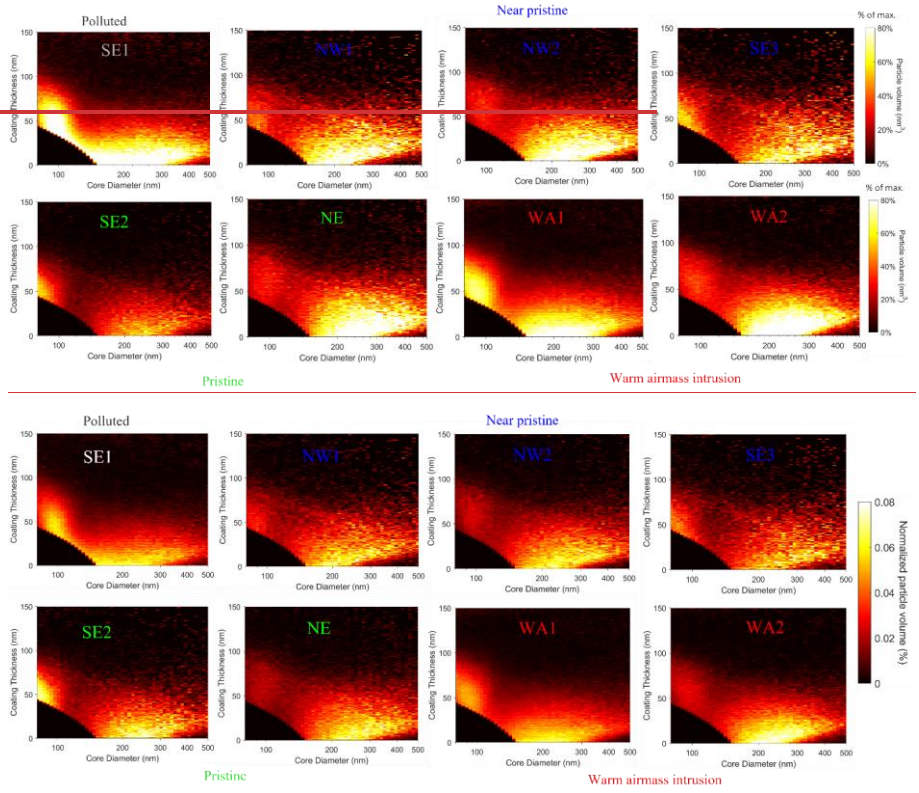

765

Figure 8: Size resolved coating thickness of rBC particles during the campaign. The colour bar indicates the particle volume normalized with the integrated total volume (in %) in each size bin.

~~**Figure 7:** Size segregated coating thickness of rBC particles during the campaign. The colour bar indicates the particle volume (in percentage) in each size bin.~~

770 During ~~the~~ WA1, the median CT is ~12 nm. This suggests that warm air mass intrusions have a notable influence on the coating of rBC particles, as evidenced by the difference in CT between SE2 (prior to the warm air mass intrusion) and WA1. This difference could be attributed to the presence of aged rBC particles transported into the central Arctic during these intrusions from biomass-burning sources, as discussed before. During WA2, as the ship re-entered the marginal ice zone, it was influenced by a ~~short-lived~~ warm airmass advection from the 775 southeast, which primarily passed over oceanic regions. The estimated median CT during this period is ~15 nm, ~~which is relatively high compared to WA1~~. Interestingly, during the second warm airmass intrusion, the prevailing air-masses shifted from north-easterly to south-easterly, which could have contributed to the observed changes in coating thickness. CT, along with a relatively higher contribution of airmasses traversing open oceanic regions, suggests relatively aged rBC particles during WA2. This could have significantly influenced the observed changes 780 in CT between WA2 and WA1, where continental emissions and biomass-burning sources were more prominent. In addition, we noticed that the mass fractions of SO_4^{2-}, NH_4^+, MSA, and $C_2O_4^{2-}$ were higher during WA2 than

Formatted: Font: 10 pt, English (United Kingdom)

Formatted: Font: 10 pt, English (United Kingdom)

Formatted: Space After: 8 pt

Formatted: Font: 10 pt, English (United Kingdom)

Formatted: Font: 10 pt, English (United Kingdom)

during WA1. Further, we found significant correlations between NH_4^+ and SO_4^{2-} (R^2=0.5), SO_4^{2-} and MSA (R^2=0.4), $C_2O_4^{2-}$ and NO_3^- (R^2=0.6), ~~indicating significant~~suggesting enhanced secondary aerosol~~ SOA~~ formation/photochemical aging ~~of aerosols~~ during this period. Consistent with this, Arun et al. (2021; and references therein) reported substantial organic aerosol formation and photochemical aging in a remote environment over the Eastern Himalayas. ~~This~~ These findings further support~~s~~ the aged nature of the aerosols during WA2, which ~~are~~ likely ~~to have~~ contributed to the relatively high~~er~~ CT during WA2.

Despite evidence of long-range transport, rBC particles ~~exhibited~~ in this study showed thin to moderate coatings, unlike previous observations in background environments with thickly coated rBC particles (Motos et al., 2020; Yang et al., 2025; Pan et al., 2026). This infers lower precursor gas concentrations and limited condensation under summer Arctic conditions, where clean background air and reduced SOA formation can suppress coating even on aged rBC particles. Additionally, in-cloud and below-cloud scavenging, especially during the prevalent fog and low-level cloud conditions of Arctic summer, likely play a significant role in removing hydrophilic or heavily coated rBC particles. ~~Although photochemical activity does occur in summer, t~~The persistent presence of clouds and fog enhances wet scavenging, which ~~disproportionately affects more processed~~significantly influence the rBC properties ~~aerosols~~. This effect is particularly evident in our observations from warm air-mass intrusions (WA1), which, despite being associated with biomass burning and continental sources, showed significantly larger rBC cores (MMD > 260 nm) but surprisingly thinner coatings than background air-masses, such as those from the NE and NW sectors. These background regimes, dominated by air-masses traversing marine or consolidated sea-ice regions, featured moderately large rBC cores (MMD ~220 nm) with moderate coatings, suggesting the combined influence of aerosol aging and active wet scavenging. The lower coating thickness~~es~~ observed in the southeast sectors (e.g., SE2), despite large MMDs, indicate that particle aging alone does not ~~guarantee~~ necessarily lead to thicker coatings; rather, prevailing environmental conditions, such as low oxidant levels or cleaner marine airmasses, can suppress formation of coating on rBC particles. Coating thickness may also be modulated by the available condensation sink. Under high particle number conditions, condensable material can be distributed across a larger population, potentially limiting per-particle coating growth even when precursors are present. Although we cannot quantify this effect here because SP2 number concentrations represent only BC-containing particles within the instrument's detection range (and not the full aerosol population), this mechanism could also contribute to the relatively low CT observed during high loading regimes such as WA1.

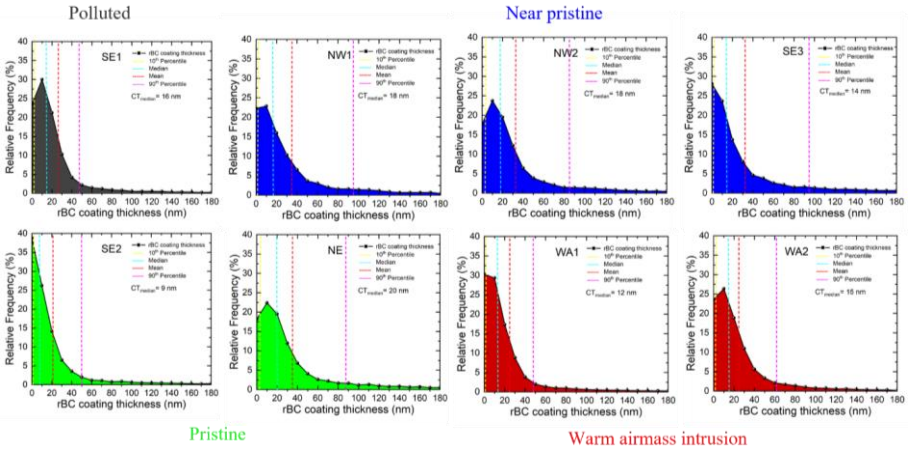

Figure ~~8~~9: Frequency distribution of the coating thickness histograms during the study period for each airmass regimes for the rBC core size range of 180-300 nm.

3.5 Light absorption enhancement of rBC particles

To understand the role of microphysical properties and mixing state ~~on~~ in modulating BC light absorption ~~enhancement~~, we ~~have~~ quantified the light absorption enhancement (E_{abs}) and mass absorption cross-section (MAC) of rBC particles using core-shell Mie theory, constrained by our in-situ single-particle observations obtained using SP2 as ~~discussed~~ described in section 2.2. In this method, E_{abs} ~~quantifies~~ represents the increase in light absorption ~~due to the presence of non-absorbing coatings on BC particles~~by coated rBC~~,~~ relative to uncoated (bare) BC~~.~~, while MAC provides the corresponding absorption efficiency per unit rBC mass. For smaller core sizes, even modest coatings can result in substantial enhancement due to the strong lensing effect. However, as the core size increases, the relative impact of coatings on absorption enhancement diminishes. Figure S6 shows the size-resolved E_{abs} and MAC of rBC particles across the different airmass regimes. In the following discussion, we focus on the ranges defined by the 80-500 nm and 180-300 nm core size intervals. The size range 80 nm to 500 nm indicates the upper limit of E_{abs} and MAC, possibly overestimated due to the missing part of mixing state information in the lower size ranges as discussed. Similarly, the 180-300 nm size range corresponds to the lower range of E_{abs} and MAC values in this study. The size-resolved E_{abs} values ranged from approximately 1.0 to 1.6 during the study period (Figure 10). ~~Figure 9 presents the size-resolved E_{abs} and MAC of rBC particles during the study period.~~

Formatted: Subscript

Formatted: Subscript

~~Across all air mass regimes, the size segregated E_{abs} values range from ~1 to 2.8 (Figure A5). The absolute magnitude of Eabs and MAC values discussed here now will focus on the size range from 80 nm to 500 nm and 180 nm to 300 nm. The size range 80 nm to 500 nm indicates the upper limit of E_{abs} and MAC possibly over estimated due to the missing part of mixing state information in the lower size ranges as discussed. The size range of 180-300 nm indicates the lower range of corresponding E_{abs} and MAC values.~~

During the polluted ~~-~~initial phase of the campaign, when the sampled airmasses were influenced predominantly by continental and anthropogenically processed sources, ~~E_{abs}~~ ranged from ~~~1.1 to 1.4 (Figure 10a), with~~ corresponding MAC values of ~~6.6-~~8.0 $m^2 g^{-1}$ (Figure 10b). These MAC values are comparable to those reported for anthropogenically influenced environments, including ~6.5 $m^2 g^{-1}$ in South China, ~7.5 $m^2 g^{-1}$ in California, ~8.4 $m^2 g^{-1}$ in Karlsruhe, and ~7.0 $m^2 g^{-1}$ during ACE-Asia flight measurements (Lan et al., 2013; Cappa et al., 2019; Linke et al., 2016; Clarke et al., 2004), indicating moderate absorption enhancement under polluted conditions. They are, however, lower than values reported for the regions such as ~9.5–10.4 $m^2 g^{-1}$ at Nordic background sites, ~11.8 $m^2 g^{-1}$ in Nanjing, and ~12.3 $m^2 g^{-1}$ at Jeju Island (Zanatta et al., 2016; Ma et al., 2020; Kondo et al., 2009).

Interestingly, during WA1, despite the predominant influence of biomass-burning emissions, both E_{abs} (~1.0-1.2) and MAC (~6.5–8.0 $m^2 g^{-1}$) remained relatively low, even lower than those observed under pristine/background Arctic conditions (E_{abs} ~1.1–1.6; MAC ~6.5–8.7 $m^2 g^{-1}$). This is notable because biomass-burning-influenced aerosols often exhibit substantially stronger absorption enhancement and higher MAC after atmospheric aging. For example, previous studies have reported E_{abs} values of ~1.38 during biomass-burning events in Boulder, ~1.5 in the Pearl River Delta, and synthesis-based values of ~1.83 for biomass-burning smoke globally (Lack et al., 2012; Wu et al., 2018; Asmi et al., 2025). Similarly, MAC values of ~13.3 $m^2 g^{-1}$ in Texas biomass-burning plumes and a global mean of ~14.7 $m^2 g^{-1}$ for biomass-burning conditions are considerably higher than those observed here (Schwarz et al., 2008; Asmi et al., 2025). Although reduced coating thickness during WA1 is consistent with lower absorption enhancement, caution should be taken against interpreting WA1 as being controlled solely by a limited coating to low E_{abs} mechanism. For Arctic transport events, the observed E_{abs} likely reflects a combination of constrained atmospheric processing (limited aging and coating) and source-related differences in rBC properties. In particular, differences in rBC composition, morphology/internal structure, and particle scale mixing heterogeneity can reduce absorption efficiency and/or make core-shell Mie-based representations less effective or less representative.

In contrast, WA2 exhibited somewhat higher enhancement, with E_{abs} increasing to ~1.1-1.5, indicating more extensive atmospheric processing and thicker coatings acquired during long-range transport. Such aging likely promoted condensation of secondary species and enhanced internal mixing, thereby increasing absorption via the lensing effect. The higher E_{abs} during WA2 compared with WA1 suggests that the radiative effects of rBC in the central Arctic depend not only on source type, but also strongly on the extent of atmospheric processing during transport. In this context, coating thickness (CT) serves as an important proxy for particle aging and internal mixing state, both of which directly modulate absorption enhancement. The contrast between WA1 and WA2 therefore highlights the importance of size-resolved coating information for interpreting variability in rBC optical properties across different airmass regimes.

~~conditions during the initial phase of the campaign, E_{abs} ranges is ~1.1 - 1.4 (Figure 9a) influenced predominantly by continental or anthropogenically processed air masses. The corresponding estimated MAC range from 6.6 - 8 $m^2 g^{-1}$ (Figure 9b). Interestingly, the light absorption enhancement of rBC and MAC remained low during warm-air-mass intrusions with predominant influence of biomass burning/gas flare emissions during WA1 (E_{abs} ~1 - 1.2, MAC ~ 6.5 - 8) than under pristine background conditions (E_{abs} ~1.1 - 1.6, MAC ~ 6.5- 8.7), underscoring a strong~~

Formatted: Subscript

Formatted: Subscript

Formatted: Subscript

Formatted: Subscript

Formatted: Subscript

Formatted: Subscript

~~dependence of rBC radiative effects in the central Arctic on source regions and aging/processing during long-range transport. The estimated E_{abs} during WA2 with significantly processed aged rBCs are higher than those during WA1 (~1.1 – 1.5). This suggests that the rBC particles during WA2 were likely more photochemically aged, acquiring thicker coatings through prolonged exposure to condensable vapors as they traveled across pristine Arctic regions. Such aging processes promote the formation of secondary aerosols and internal mixing, ultimately enhancing light absorption even in relatively clean air masses. The observed tendencies emphasize the importance of CT as a proxy for particle aging and internal mixing, both of which directly influence absorption enhancement via the lensing effect. These observations indicate that, even with limited aging and reduced condensation of secondary species during transport through relatively clean environments, warm air mass intrusions carrying biomass-burning plumes can enhance light absorption in the Arctic marine boundary layer. However, between the two warm air mass intrusion cases, WA2 showed an even higher E_{abs} than WA1, due to the more aged aerosol conditions. The size resolved coating information on rBC particles is therefore essential for interpreting the degree of rBC aging across different air mass regimes.~~

It is worth noting that the estimated E_{abs} values in this study are comparable with earlier field observations, including ~1.06 in California (Cappa et al., 2012), ~1.06 at an east Asian outflow site Noto Peninsula (Ueda et al., 2016), ~1.38 during biomass burning events in Boulder (Lack et al., 2012), 1.50 ± 0.48 in the Pearl River Delta (Wu et al., 2018), ~1.36 for marine airmass periods to ~1.58 for the continental airmass periods over a tropical coastal site (Nithin et al., 2026), ~ 1.15 in Beijing (Liu et al., 2020), and ~1.69 in Shanghai (Zhai et al., 2022), ~1.42 Nanjing in China (Ma et al., 2020), 1.1-1.3 in a background site in the Qinghai-Tibet Plateau (Zeng et al. 2024). Larger values approaching or exceeding 2 have been observed in strongly aged or biomass-burning-influenced aerosol, such as pyrocumulonimbus plumes and remote high-altitude environments (Beeler et al., 2024; Tinorua et al., 2024). Zhang et al. (2023) also reported E_{abs} in the range of ~1.2-2.0 with higher E_{abs} for fully coated BC in North China Plain. Utilizing the global measurements, Asmi et al., (2025; and references therein) reported average E_{abs} for the urban and remote environments as 1.38 and 1.59 respectively as well as Eabs ~1.8-3.0 for the biomass burning smoke. Laboratory evidence also indicates that coatings can substantially enhance BC absorption. Shiraiwa et al. (2010) found an approximately 2-fold increase in absorption for BC coated with oleic acid and glycerol, while Khalizov et al. (2009) reported an Eabs of around 1.4 after sulfuric acid condensation on black carbon. These previous studies collectively indicate that most atmospheric E_{abs} values fall in the range of about 1.0-2.0 under typical ambient conditions, while higher values are generally associated with extensive aging, thicker coatings, or biomass-burning influence. It is important to note, however, that E_{abs} values reported in the literature are derived using different methodological approaches, including core-shell Mie theory, thermodenuder coupled with photoacoustic absorption measurements, filter-based methods, and optical approaches combining cavity ring-down spectroscopy and nephelometry. Similarly, MAC values have been derived using different combinations of absorption measurements and BC mass quantification, such as PSAP or photoacoustic absorption together with EC, SP2, SP-AMS, or COSMOS measurements. These methodological differences can contribute to inter-study variability and should be considered when comparing absolute values across regions and source regimes. Table S1 and Table S2 providing an overview of the E_{abs} and MAC values and methods used in previous studies in comparison with our observaitons. It is important to note that the E_{abs} values reported here are based on a core-shell Mie theory that assumes a spherical BC core fully encapsulated by non-absorbing coating material. Ambient rBC particles, however, often exhibit fractal/irregular morphologies, partial coating, and mixing state

Formatted: Font: (Default) Times New Roman, 10 pt, Not Bold, Font color: Auto

Formatted: Line spacing: 1.5 lines

Formatted: Font: (Default) Times New Roman, 10 pt, Not Bold, Font color: Auto

heterogeneity. As a result, core-shell-based E_{abs} may represent an upper-bound or idealized estimate of absorption enhancement relative to more realistic particle representations (e.g., Adachi et al., 2010; Ueda et al., 2016; Fierce et al., 2020; Liu et al., 2020; Zhai et al., 2022; Romshoo et al., 2025). Overall, the present results indicate that most E_{abs} values in the central Arctic fall within the lower to moderate range reported for ambient atmospheric conditions, and that the variability between regimes is primarily controlled by the combined influence of source characteristics, atmospheric aging, removal processes, and mixing state.

Formatted: Font: (Default) Times New Roman, 10 pt, Not Bold, Font color: Auto

Formatted: English (United Kingdom)

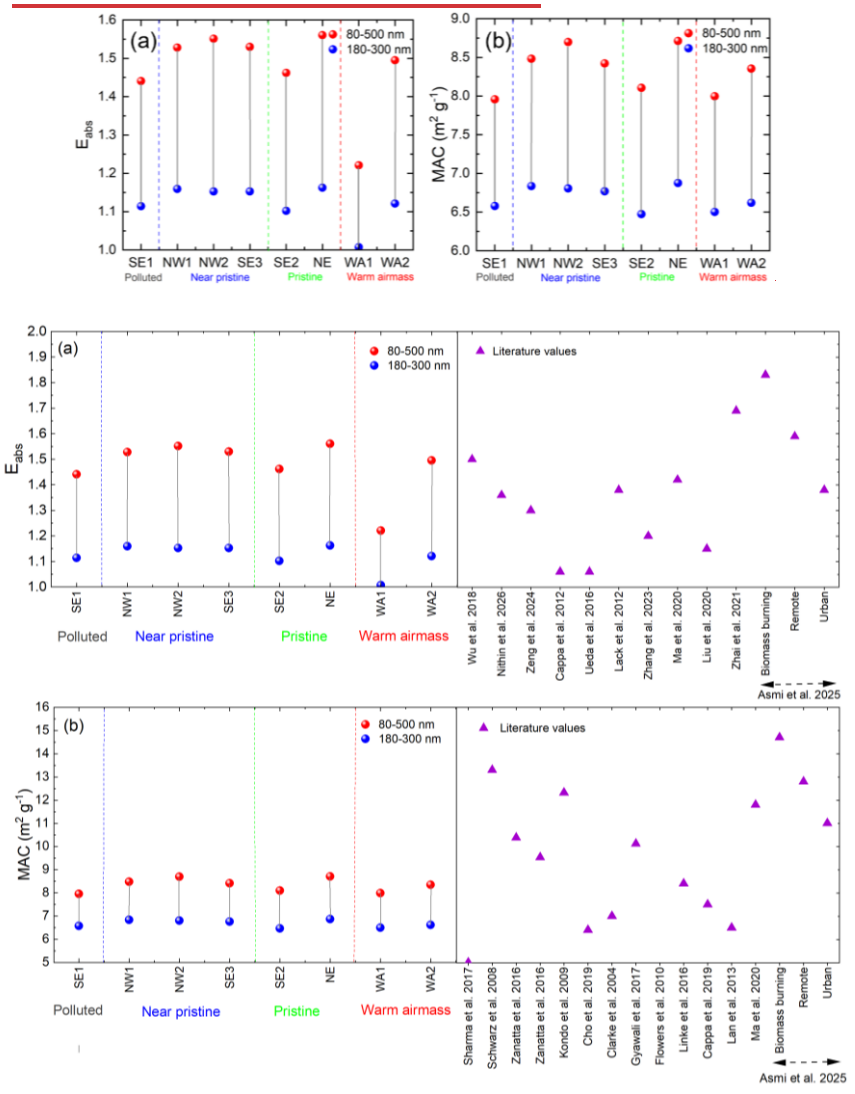

Figure 910: (a) Estimated absorption enhancement (E_{abs}) and mass absorption cross section of refractory black carbon particles for each regime for the rBC core size ranges, (a) 80-500 nm and, (b) 180-300 nm. (b) Estimated mass absorption cross section of refractory black carbon particles for each regime for the rBC core size ranges,80-500 nm and180-300 nm.

Formatted: Font: (Default) Times New Roman, 10 pt, Not Bold, Font color: Auto, English (United States)

The size-resolved variation in E_{abs}, MAC, and coating thickness across different air masses hashave critical implications for understanding the radiative impacts of BC in the Arctic. Highly coated BC particles can significantly increase shortwave radiation absorption, contributing to local atmospheric warming and potential feedbacks through snow and sea-ice albedo reduction. The pronounced absorption enhancement observed during WA1 suggests that continental or anthropogenically influenced air masses, though less frequent, can be major contributors to BC radiative forcing in the Arctic MBL. Nonetheless, several limitations should be acknowledged. Mie theory, used for estimating E_{abs} assumes spherical core-shell morphology, which may not accurately capture the irregular or fractal shapes of ambient BC aggregates, particularly in fresh emissions. Moreover, the composition of the coatings, especially the presence of light-absorbing organics such as brown carbon, is not explicitly resolved in MAC calculations, though it can substantially influence absorption. Overall, theThe observed heterogeneity in rBC optical properties across air mass regimes underscores the need for dynamic, region-specific parameterizations in climate models. Relying on constant enhancement factors or bulk MAC values across different transport conditions risks oversimplifying the real variability. It could lead to significant uncertainties in estimates of BC direct radiative forcing. The strong link between coating thickness and radiative properties further underscores the importance of accurately capturing aerosol aging processes when modeling BC's role in the Arctic climate. These findings provide essential observational constraints for climate models and underscore the need to incorporate rBC mixing state and size-resolved properties into Arctic radiative effect assessments.

4. Conclusion

To understand the microphysical properties and mixing state ofinvestigate the microphysical properties and mixing state of atmospheric refractory black carbon (rBC) particles aerosols in the central Arctic marine boundary layer, measurements werewe conducted measurements on board the RV *Polarstern* during the ATWAICE campaign in summer 2022. This study provides new insights into the spatial and temporal variability of rBC properties including its abundance, size distribution, mixing state, microphysical properties, mixing state, and radiative behavior properties of rBC aerosols in the central Arctic marine boundary layer during the summer melt season. We examined the characteristics of rBC particles across a range of synoptic regimes defined by air mass source regions, surface types, and transport histories. Our results reveal that air mass origin and atmospheric processing strongly govern rBC abundance, size, and coating characteristics.Our results reveal that airmass transport pathways, atmospheric processing and removal mechanisms strongly influence rBC abundance, its size distribution, and mixing state in the summertime central Arctic marine boundary layer.

rBC mass concentrations, size distributions, and coating thickness varied substantially across the different transport regimes considered in this study. The lowest rBC mass concentrations were observed under pristine and near-pristine conditions, typically on the order of ~0.4- 0.6 ng m^{-3}. In contrast warm airmass intrusions into the

Formatted: Superscript

central Arctic were associated with clear enhancements in rBC, with maximum concentrations reaching ~74 ng m^{-3} during WA1. These results demonstrate that episodic transport from lower latitudes can strongly perturb the otherwise low-aerosol summertime Arctic background. Further, the higher rBC during WA1 is found to associated with significant influences from the biomass burning sources during the warm airmass intrusion.

The mass median diameter (MMD) of rBC varied substantially across the different transport regimes with a clear latitudinal shift in the mass median diameter (MMD) of rBC from the lower latitude near coastal marine environments (~156 nm) to the high latitudes of the central Arctic (~220 nm). The particularly high MMD observed during WA1 (>260 nm) indicates that warm-air intrusions can substantially modify the microphysical properties of rBC in the central Arctic. The observed variability in MMD is interpreted as reflecting the combined effects of source influence, airmass transport pathways, and atmospheric processing during long-range transport, rather than a unique signature of emission source alone. The mixing state of rBC showed similarly strong regime dependence. The size-resolved mixing state revealed pronounced heterogeneity, with non-BC material distributed unevenly across rBC particles of different core sizes. Airmasses with higher continental influence generally exhibited enhanced rBC concentrations and distinct coating characteristics relative to the clean marine and sea-ice influenced regimes. At the same time, the observed coating thickness were often lower than that might be expected for aged particles transported over long distances.

~~rBC mass concentrations, size distributions, and coatings varied distinctly across synoptic regimes, from continental and biomass-burning influenced air masses with higher concentrations and larger cores to pristine marine regimes with extremely low rBC loadings and moderately coated particles. Despite long-range transport, coatings on rBC particles remained unexpectedly lower, likely due to limited condensable material, weak secondary aerosol formation, and efficient wet scavenging in the humid Arctic boundary layer. The limited availability of condensable material, reduced secondary aerosol formation, and the frequent occurrence of persistent fog and low-level clouds likely contribute to the observed thinner coatings. Furthermore, efficient in-cloud and below-cloud scavenging of heavily coated, hydrophilic particles may further reduce the coating thickness within the observed rBC population. The observed contrasts between continental, marine, and biomass-burning influenced warm air masse intrusions emphasize that rBC aging and internal mixing are highly nonuniform under Arctic summer conditions.~~

~~Regions influenced by south easterly air mass advection, characterized by stronger continental influence, exhibited relatively higher coating thicknesses for smaller rBC cores. In contrast, northerly advections associated with pristine marine environments were dominated by larger rBC particles, which also showed comparatively higher coating thicknesses. Air masses affected by continental outflows and biomass burning (particularly during warm airmass intrusion, WA1) carried elevated rBC concentrations and displayed larger mass median diameters (MMDs, ~264 nm). In comparison, air masses that primarily traversed the central Arctic Ocean and consolidated sea ice regions (NE) reflected near pristine conditions, with minimal rBC concentrations (<0.6 ng m^{-3}) and only moderately coated particles. The open oceanic regimes (SE2, SE3) exhibited intermediate characteristics, indicating rBC populations that were relatively aged and moderately coated, likely shaped by extended atmospheric residence times and interactions within the marine boundary layer. The clear contrast between~~

Formatted: Superscript

Formatted: Font: English (United Kingdom), Not Highlight

Formatted: Font: English (United Kingdom)

Formatted: Font: English (United Kingdom), Not Highlight

Formatted: Font: English (United Kingdom)

Formatted: Font: English (United Kingdom)

Formatted: Font: (Default) Times New Roman, English (United States)

Formatted: English (United States)

Formatted: Font: English (United Kingdom)

Formatted: Space Before: 12 pt, After: 8 pt

~~biomass burning/gas flaring influenced air masses (e.g., WA1) and pristine marine regimes (e.g., NE) highlights that even aged rBC particles can remain only partially internally mixed under Arctic summer conditions.~~

The size-resolved analysis of light absorption ~~properties of individual rBC particles~~properties based on the core-shell Mie theory further showed ~~revealed~~ substantial variability in both the absorption enhancement ~~factor~~ (E_{abs}) and the mass absorption cross-section (MAC). The size-resolved E_{abs} values ranged from approximately 1.0 - 1.6 across all airmass regimes. The pristine and near-pristine regimes exhibited comparatively high E_{abs} and MAC values, consistent with more internally mixed and atmospherically processed particles. In contrast, WA1 showed comparatively low E_{abs} (generally <1.1) despite enhanced rBC concentrations, indicating that the particles transported during this event were not necessarily highly coated. By comparison, WA2 exhibited higher E_{abs} than WA1, with weaker evidence of direct combustion influence~~,~~. This contrast indicates that the radiative properties of rBC in the Arctic are governed not only by source region but also by airmass transport pathways, as passage over marine or relatively cleaner environments may promote prolonged aging and a greater influence of secondarily processed aerosol on the mixing state of rBC. ~~parameters that are highly sensitive to the degree of internal mixing and coating thickness. The near pristine and pristine regimes, exhibited elevated E_{abs} and MAC, indicative of more internally mixed or aged particles. In contrast, the biomass burning influenced regime WA1, associated with warm air mass intrusions, showed comparatively lower $E_{abs,}$ suggesting the presence of less aged particles or limited secondary processing during transport. Interestingly, the WA2 regime, though not directly influenced by biomass burning, showed higher E_{abs} than WA1, suggesting that the nature of the airmass transport pathway, particularly its passage over marine or relatively clean environments, can facilitate prolonged aging and coating development even in the absence of strong primary sources.~~

~~These findings highlight the complex behavior of rBC in the summer Arctic, modulated by the interplay of atmospheric transport and source characteristics~~. The results emphasize that fixed~~,~~ or generalized MAC or E_{abs} are unlikely to adequately represent ~~values are inadequate for~~ Arctic conditions. Instead, regime-specific~~,~~ sizeand size-resolved representations that account for ~~, and~~ mixing- state and atmospheric aging conditions are needed to improve model descriptions of BC radiative effects in the Arctic. ~~dependent representations are essential for improving model accuracy.~~ Given the high climatic sensitivity of the Arctic to light absorbing aerosols perturbations, improved characterization of rBC abundance, size and mixing state heterogeneity is essential for reducing uncertainties in estimates of aerosol radiative forcing and Arctic~~Arctic's high sensitivity to radiative forcing from absorbing aerosols, accurate characterization of rBC microphysical properties is vital for reducing uncertainties in~~ climate projections.

Acknowledgement

We gratefully acknowledge the funding by the German Research Foundation, DFG grants WE 2757/6-1 and HE 5214/10-1. We gratefully acknowledge the funding by the Deutsche Forschungsgemeinschaft (DFG, German Research Foundation) through the Transregional Collaborative Research Centre TRR-172 'ArctiC Amplification: Climate Relevant Atmospheric and SurfaCe Processes, and Feedback Mechanisms (AC)^3' (grant 268020496). We thank Dr. Heike Wex and Dr. Holger Siebert (Leibniz Institute for Tropospheric Research, Germany) for the helpful suggestions and comments on improving this paper. We also thank Dr. Bruna A. Holanda (Hessian Agency

Formatted: Subscript
Formatted: Subscript
Formatted: Subscript
Formatted: Subscript
Formatted: Font: (Default) Times New Roman, 10 pt, English (United States)
Formatted: Font: (Default) Times New Roman, 10 pt, English (United States)
Formatted: Superscript

for Nature Conservation, Environment and Geology, Germany) for her support during this study. We thank everyone involved in the expedition of the research vessel *Polarstern* during ATWAICE in 2022 (Grant No. AWI_PS131_11 (Alfred-Wegener-Institut Helmholtz-Zentrum für Polar-und Meeresforschung, 2017). We thank the Institute of Environmental Physics, University of Bremen, for the provision of the merged MODIS-AMSR2 sea-ice concentration data at https://data.seaice.uni-bremen.de/modis_amsr2 (last access 15.10.2023). We acknowledge the use of Grammarly during the preparation of this paper. We thank Prof. Dr. Torsten Kanzow and the ATWAICE team for their support during the campaign.

Data availability

Data are available upon request from the corresponding author (arun.babu@tropos.de).

Competing Interests

At least one of the (co-) authors is a member of the editorial board of Atmospheric Chemistry and Physics.

Author contributions

BSA, TM, MLP, BW conceptualized the study. BSA, SL, PO conducted onboard measurements. BSA, TM, MvP performed data processing. AW, JR provided the radiometer datasets. BSA prepared the original draft of the paper. All authors contributed to reviewing and editing the manuscript.

References

Adachi, K., Chung, S. H., and Buseck, P. R.: Shapes of soot aerosol particles and implications for their effects on climate, Journal of Geophysical Research Atmospheres, 115, https://doi.org/10.1029/2009JD012868, 2010.

Arun, B. S., Aswini, A. R., Gogoi, M. M., Hegde, P., Kumar Kompalli, S., Sharma, P., and Suresh Babu, S.: Physico-chemical and optical properties of aerosols at a background site (~4 km a.s.l.) in the western Himalayas, Atmos. Environ., 218, https://doi.org/10.1016/j.atmosenv.2019.117017, 2019.

Arun, B. S., Gogoi, M. M., Hegde, P., Borgohain, A., Boreddy, S. K. R., Kundu, S. S., and Babu, S. S.: Carbonaceous Aerosols over Lachung in the Eastern Himalayas: Primary Sources and Secondary Formation of Organic Aerosols in a Remote High-Altitude Environment, ACS Earth Space Chem., 5, 2493–2506, https://doi.org/10.1021/acsearthspacechem.1c00190, 2021.

Arctic Monitoring and Assessment Programme (AMAP) AMAP Assessment 2015: Black carbon and ozone as Arctic climate forcers.

Asmi, E., Backman, J., Servomaa, H., Virkkula, A., Gini, M. I., Eleftheriadis, K., Müller, T., Ohata, S., Kondo, Y., and Hyvärinen, A.: Absorption instruments inter-comparison campaign at the Arctic Pallas station, Atmos Meas Tech, 14, 5397-5413, https://doi.org/10.5194/amt-14-5397-2021, 2021.

Asmi, E., Sipkens, T. A., Saturno, J., Backman, J., Vasilatou, K., Weingartner, E., Keller, A., Ciupek, K., Müller, T., Babu Suja, A., Močnik, G., Drinovec, L., Eleftheriadis, K., Gini, M. I., Nowak, A., and Corbin, J. C.: Mass absorption cross-section of ambient black carbon aerosols - a review, NPJ Clim Atmos Sci, https://doi.org/10.1038/s41612-025-01288-2, 2025.

Backman, J., Schmeisser, L., Virkkula, A., Ogren, J. A., Asmi, E., Starkweather, S., Sharma, S., Eleftheriadis, K., Uttal, T., Jefferson, A., Bergin, M., Makshtas, A., Tunved, P., and Fiebig, M.: On Aethalometer measurement uncertainties and an instrument correction factor for the Arctic, Atmos Meas Tech, 10, 5039-5062, https://doi.org/10.5194/amt-10-5039-2017, 2017.

Baumgardner, D., Popovicheva, O., Allan, J., Bernardoni, V., Cao, J., Cavalli, F., Cozic, J., Diapouli, E., Eleftheriadis, K., Genberg, P. J., Gonzalez, C., Gysel, M., John, A., Kirchstetter, T. W., Kuhlbusch, T. A. J., Laborde, M., Lack, D., Müller, T., Niessner, R., Petzold, A., Piazzalunga, A., Putaud, J. P., Schwarz, J., Sheridan, P., Subramanian, R., Swietlicki, E., Valli, G., Vecchi, R., and Viana, M.: Soot reference materials for instrument calibration and intercomparisons: A workshop summary with recommendations, Atmos Meas Tech, 5, 1869-1887, https://doi.org/10.5194/amt-5-1869-2012, 2012.

Beeler, P., Kumar, J., Schwarz, J. P., Adachi, K., Fierce, L., Perring, A. E., Katich, J. M., and Chakrabarty, R. K.: Light absorption enhancement of black carbon in a pyrocumulonimbus cloud, Nature Communications, 15, https://doi.org/10.1038/s41467-024-50070-0, 2024.

Beer, E., Eisenman, I., and Wagner, T. J. W.: Polar Amplification Due to Enhanced Heat Flux Across the Halocline, Geophys Res Lett, 47, https://doi.org/10.1029/2019GL086706, 2020.

Birch, M. E. and Cary, R. A.: Elemental Carbon-Based Method for Monitoring Occupational Exposures to Particulate Diesel Exhaust, Aerosol Science and Technology, 25, 221–241, https://doi.org/10.1080/02786829608965393, 1996.

Bohren, C. F. and Huffman, D. R.: Frontmatter, in: Absorption and Scattering of Light by Small Particles, Wiley, https://doi.org/10.1002/9783527618156.fmatter, 1998.

Bond, T. C., Doherty, S. J., Fahey, D. W., Forster, P. M., Berntsen, T., Deangelo, B. J., Flanner, M. G., Ghan, S., Kärcher, B., Koch, D., Kinne, S., Kondo, Y., Quinn, P. K., Sarofim, M. C., Schultz, M. G., Schulz, M., Venkataraman, C., Zhang, H., Zhang, S., Bellouin, N., Guttikunda, S. K., Hopke, P. K., Jacobson, M. Z., Kaiser, J. W., Klimont, Z., Lohmann, U., Schwarz, J. P., Shindell, D., Storelvmo, T., Warren, S. G., and Zender, C. S.: Bounding the role of black carbon in the climate system: A scientific assessment, Journal of Geophysical Research Atmospheres, 118, 5380–5552, https://doi.org/10.1002/jgrd.50171, 2013.

Bozem, H., Hoor, P., Kunkel, D., Köllner, F., Schneider, J., Herber, A., Schulz, H., Richard Leaitch, W., Aliabadi, A. A., Willis, M. D., Burkart, J., and Abbatt, J. P. D.: Characterization of transport regimes and the polar dome

Formatted: Font: (Default) Times New Roman, 10 pt, Font color: Auto

Formatted: Font: (Default) Times New Roman, 10 pt, Font color: Auto

during Arctic spring and summer using in situ aircraft measurements, Atmos Chem Phys, 19, 15049–15071, https://doi.org/10.5194/acp-19-15049-2019, 2019.

Cappa, C. D., Onasch, T. B., Massoli, P., Worsnop, D. R., Bates, T. S., Cross, E. S., Davidovits, P., Hakala, J., Hayden, K. L., Jobson, B. T., Kolesar, K. R., Lack, D. A., Lerner, B. M., Li, S. M., Mellon, D., Nuaaman, I., Olfert, J. S., Petäjä, T., Quinn, P. K., Song, C., Subramanian, R., Williams, E. J., and Zaveri, R. A.: Radiative absorption enhancements due to the mixing state of atmospheric black carbon, Science (1979)., 337, 1078–1081, https://doi.org/10.1126/science.1223447, 2012.

Cappa, C. D., Zhang, X., Russell, L. M.,Collier, S., Lee, A. K. Y., Chen, C.-L., etal. (2019). Light absorption by ambientblack and brown carbon and itsdependence on black carbon coatingstate for two California, USA, cities inwinter and summer. Journal ofGeophysical Research: Atmospheres,124, 1550–1577. https://doi.org/10.1029/2018JD029501.

Ching, J., Riemer, N., and West, M.: Black carbon mixing state impacts on cloud microphysical properties: Effects of aerosol plume and environmental conditions, J Geophys Res, 121, 5990-6013, https://doi.org/10.1002/2016JD024851, 2016.

Ching, J., West, M., and Riemer, N.: Quantifying impacts of aerosol mixing state on nucleation-scavenging of black carbon aerosol particles, Atmosphere (Basel), 9, https://doi.org/10.3390/atmos9010017, 2018.

Cho, C., Kim, S. W., Lee, M., Lim, S., Fang, W., Gustafsson, Ö., Andersson, A., Park, R. J., and Sheridan, P. J.: Observation-based estimates of the mass absorption cross-section of black and brown carbon and their contribution to aerosol light absorption in East Asia, Atmos. Environ., 212, 65–74, https://doi.org/10.1016/j.atmosenv.2019.05.024, 2019.

Clarke, A. D., Shinozuka, Y., Kapustin, V. N., Howell, S., Huebert, B., Doherty, S., Anderson, T., Covert, D., Anderson, J., Hua, X., Moore, K. G., McNaughton, C., Carmichael, G., and Weber, R.: Size distributions and mixtures of dust and black carbon aerosol in Asian outflow: Physiochemistry and optical properties, Journal of Geophysical Research D: Atmospheres, 109, https://doi.org/10.1029/2003JD004378, 2004.

Croft, B., Martin, R. V., Richard Leaitch, W., Tunved, P., Breider, T. J., D'Andrea, S. D., and Pierce, J. R.: Processes controlling the annual cycle of Arctic aerosol number and size distributions, Atmos Chem Phys, 16, 3665–3682, https://doi.org/10.5194/acp-16-3665-2016, 2016.

Dada, L., Angot, H., Beck, I., Baccarini, A., Quéléver, L. L. J., Boyer, M., Laurila, T., Brasseur, Z., Jozef, G., de Boer, G., Shupe, M. D., Henning, S., Bucci, S., Dütsch, M., Stohl, A., Petäjä, T., Daellenbach, K. R., Jokinen, T., and Schmale, J.: A central arctic extreme aerosol event triggered by a warm air-mass intrusion, Nat Commun, 13, https://doi.org/10.1038/s41467-022-32872-2, 2022.

Dekoutsidis, G., Wirth, M., and Groß, S.: The effects of warm-air intrusions in the high Arctic on cirrus clouds, Atmos Chem Phys, 24, 5971–5987, https://doi.org/10.5194/acp-24-5971-2024, 2024.

Eleftheriadis, K., Vratolis, S., and Nyeki, S.: Aerosol black carbon in the European Arctic: Measurements at Zeppelin station, Ny-Ålesund, Svalbard from 1998-2007, Geophys Res Lett, 36, https://doi.org/10.1029/2008GL035741, 2009.

Engvall, A.-C., Krejci, R., Ström, J., Treffeisen, R., Scheele, R., Hermansen, O., and Paatero, J.: Changes in aerosol properties during spring-summer period in the Arctic troposphere, Atmos. Chem. Phys, 445–462 pp., 2008.

Fierce, L., Riemer, N., and Bond, T. C.: Explaining variance in black carbon's aging timescale, Atmos Chem Phys, 15, 3173–3191, https://doi.org/10.5194/acp-15-3173-2015, 2015.

Fierce, L., Bond, T. C., Bauer, S. E., Mena, F., and Riemer, N.: Black carbon absorption at the global scale is affected by particle-scale diversity in composition, Nat Commun, 7, https://doi.org/10.1038/ncomms12361, 2016.

Fierce, L., Onasch, T. B., Cappa, C. D., Mazzoleni, C., China, S., Bhandari, J., Davidovits, P., Al Fischer, D., Helgestad, T., Lambe, A. T., Sedlacek, A. J., Smith, G. D., and Wolff, L.: Radiative absorption enhancements by black carbon controlled by particle-to-particle heterogeneity in composition, Proc Natl Acad Sci U S A, 117, 5196–5203, https://doi.org/10.1073/pnas.1919723117, 2020.

Formatted: Font: (Default) Times New Roman, 10 pt, Font color: Auto

Formatted: Font: (Default) Times New Roman, 10 pt

Formatted: Font: (Default) Times New Roman, 10 pt, Font color: Auto

Formatted: Font: (Default) Times New Roman, 10 pt, Font color: Auto

Formatted: Font: (Default) Times New Roman, 10 pt, Font color: Auto

Flanner, M. G.: Arctic climate sensitivity to local black carbon, Journal of Geophysical Research Atmospheres, 118, 1840–1851, https://doi.org/10.1002/jgrd.50176, 2013.

Flowers, B. A., Dubey, M. K., Mazzoleni, C., Stone, E. A., Schauer, J. J., Kim, S. W., and Yoon, S. C.: Optical-chemical-microphysical relationships and closure studies for mixed carbonaceous aerosols observed at Jeju Island; 3-laser photoacoustic spectrometer, particle sizing, and filter analysis, Atmos. Chem. Phys., 10, 10387–10398, https://doi.org/10.5194/acp-10-10387-2010, 2010.

Fossum, K. N., Ovadnevaite, J., Liu, D., Flynn, M., O'Dowd, C., and Ceburnis, D.: Background levels of black carbon over remote marine locations, Atmos. Res., 271, https://doi.org/10.1016/j.atmosres.2022.106119, 2022.

Gao, R. S., Schwarz, J. P., Kelly, K. K., Fahey, D. W., Watts, L. A., Thompson, T. L., Spackman, J. R., Slowik, J. G., Cross, E. S., Han, J. H., Davidovits, P., Onasch, T. B., and Worsnop, D. R.: A novel method for estimating light-scattering properties of soot aerosols using a modified single-particle soot photometer, Aerosol Science and Technology, 41, 125–135, https://doi.org/10.1080/02786820601118398, 2007.

Garrett, T. J., Brattström, S., Sharma, S., Worthy, D. E. J., and Novelli, P.: The role of scavenging in the seasonal transport of black carbon and sulfate to the Arctic, Geophys Res Lett, 38, https://doi.org/10.1029/2011GL048221, 2011.

Gogoi, M. M., Pandey, S. K., Arun, B. S., Nair, V. S., Thakur, R. C., Chaubey, J. P., Tiwari, A., Manoj, M. R., Kompalli, S. K., Vaishya, A., Prijith, S. S., Hegde, P., and Babu, S. S.: Long-term changes in aerosol radiative properties over Ny-Ålesund: Results from Indian scientific expeditions to the Arctic, Polar Sci, 30, https://doi.org/10.1016/j.polar.2021.100700, 2021.

Graham, R. M., Cohen, L., Petty, A. A., Boisvert, L. N., Rinke, A., Hudson, S. R., Nicolaus, M., and Granskog, M. A.: Increasing frequency and duration of Arctic winter warming events, Geophys Res Lett, 44, 6974–6983, https://doi.org/10.1002/2017GL073395, 2017.

Gustafsson, Ö., Budhavant, K., Chimurkar, N., Clarke, S., Dreyfus, G., Gong, X., Klimont, Z., Klingmüller, K., Kim, S. W., Lelieveld, J., Myhre, G., Nair, H. R. C. R., Peng, J., Ramanathan, V., Rana, A., Manoj, M. R., Satheesh, S. K., Venkataraman, C., and Zhang, Q.: Atmospheric black carbon in the climate system, https://doi.org/10.1038/s43017-026-00773-3, 2026.

Gyawali, M., Arnott, W. P., Zaveri, R. A., Song, C., Flowers, B., Dubey, M. K., Setyan, A., Zhang, Q., China, S., Mazzoleni, C., Gorkowski, K., Subramanian, R., and Moosmüller, H.: Evolution of multispectral aerosol absorption properties in a biogenically-influenced urban environment during the CARES campaign, Atmosphere (Basel)., 8, https://doi.org/10.3390/atmos8110217, 2017.

Haywood, J. and Boucher, O.: Estimates of the direct and indirect radiative forcing due to tropospheric aerosols, a review, 2000.

Henderson, G. R., Barrett, B. S., Wachowicz, L. J., Mattingly, K. S., Preece, J. R., and Mote, T. L.: Local and Remote Atmospheric Circulation Drivers of Arctic Change: A Review, https://doi.org/10.3389/feart.2021.709896, 1 July 2021.

Heutte, B., Bergner, N., Beck, I., Angot, H., Dada, L., Quéléver, L. L. J., Laurila, T., Boyer, M., Brasseur, Z., Daellenbach, K. R., Henning, S., Kuang, C., Kulmala, M., Lampilahti, J., Lampimäki, M., Petäjä, T., Shupe, M. D., Sipilä, M., Uin, J., Jokinen, T., and Schmale, J.: Measurements of aerosol microphysical and chemical properties in the central Arctic atmosphere during MOSAiC, Sci Data, 10, https://doi.org/10.1038/s41597-023-02586-1, 2023.

Jurányi, Z., Zanatta, M., Lund, M., Samset, B., Skeie, R., Sharma, S., and Herber, A.: A climatology of Black Carbon properties in the Arctic, from a decade of spring and summertime aircraft measurements, https://doi.org/10.21203/rs.3.rs-1938170/v1, 11 August 2022.

Jurányi, Z., Zanatta, M., Lund, M. T., Samset, B. H., Skeie, R. B., Sharma, S., Wendisch, M., and Herber, A.: Atmospheric concentrations of black carbon are substantially higher in spring than summer in the Arctic, Commun Earth Environ, 4, https://doi.org/10.1038/s43247-023-00749-x, 2023.

Formatted: Font: (Default) Times New Roman, 10 pt, Font color: Auto

Formatted: Font: (Default) Times New Roman, 10 pt, Font color: Auto

Formatted: Font: (Default) Times New Roman, 10 pt, Font color: Auto

Kanzow, T.: Berichte zur Polar- und Meeresforschung, Bericht Nr. 770/2023, https://doi.org/10.57738/BzPM_0770_2023, 2023.

Khalizov, A. F., Xue, H., Wang, L., Zheng, J., and Zhang, R.: Enhanced light absorption and scattering by carbon soot aerosol internally mixed with sulfuric acid, Journal of Physical Chemistry A, 113, 1066–1074, https://doi.org/10.1021/jp807531n, 2009.

Ko, J., Krasowsky, T., and Ban-Weiss, G.: Measurements to determine the mixing state of black carbon emitted from the 2017-2018 California wildfires and urban Los Angeles, Atmos Chem Phys, 20, 15635–15664, https://doi.org/10.5194/acp-20-15635-2020, 2020.

Kompalli, S. K., Babu, S. N. S., Krishnakumari Satheesh, S., Moorthy, K. K., Das, T., Boopathy, R., Liu, D., Darbyshire, E., Allan, J. D., Brooks, J., Flynn, M. J., and Coe, H.: Seasonal contrast in size distributions and mixing state of black carbon and its association with PM1.0 chemical composition from the eastern coast of India, Atmos Chem Phys, 20, 3965–3985, https://doi.org/10.5194/acp-20-3965-2020, 2020.

Kompalli, S. K., Babu, S. N. S., Moorthy, K. K., Satheesh, S. K., Gogoi, M. M., Nair, V. S., Jayachandran, V. N., Liu, D., Flynn, M. J., and Coe, H.: Mixing state of refractory black carbon aerosol in the South Asian outflow over the northern Indian Ocean during winter, Atmos Chem Phys, 21, 9173–9199, https://doi.org/10.5194/acp-21-9173-2021, 2021.

Kondo, Y., Sahu, L., Kuwata, M., Miyazaki, Y., Takegawa, N., Moteki, N., Imaru, J., Han, S., Nakayama, T., Oanh, N. T. K., Hu, M., Kim, Y. J., and Kita, K.: Stabilization of the mass absorption cross section of black carbon for filter-based absorption photometry by the use of a heated inlet, Aerosol Science and Technology, 43, 741–756, https://doi.org/10.1080/02786820902889879, 2009.

Laborde, M., Schnaiter, M., Linke, C., Saathoff, H., Naumann, K.-H., Möhler, O., Berlenz, S., Wagner, U., Taylor, J. W., Liu, D., Flynn, M., Allan, J. D., Coe, H., Heimerl, K., Dahlkötter, F., Weinzierl, B., Wollny, A. G., Zanatta, M., Cozic, J., Laj, P., Hitzenberger, R., Schwarz, J. P., and Gysel, M.: Single Particle Soot Photometer intercomparison at the AIDA chamber, Atmos Meas Tech, 5, 3077–3097, https://doi.org/10.5194/amt-5-3077-2012, 2012.

Laborde, M., Crippa, M., Tritscher, T., Jurányi, Z., Decarlo, P. F., Temime-Roussel, B., Marchand, N., Eckhardt, S., Stohl, A., Baltensperger, U., Prévôt, A. S. H., Weingartner, E., and Gysel, M.: Black carbon physical properties and mixing state in the European megacity Paris, Atmos Chem Phys, 13, 5831–5856, https://doi.org/10.5194/acp-13-5831-2013, 2013.

Lack, D. A., Langridge, J. M., Bahreini, R., Cappa, C. D., Middlebrook, A. M., and Schwarz, J. P.: Brown carbon and internal mixing in biomass burning particles, 109, 14802–14807, https://doi.org/10.1073/pnas.1206575109/-/DCSupplemental, 2012.

Lan, Z. J., Huang, X. F., Yu, K. Y., Sun, T. Le, Zeng, L. W., and Hu, M.: Light absorption of black carbon aerosol and its enhancement by mixing state in an urban atmosphere in South China, Atmos. Environ., 69, 118–123, https://doi.org/10.1016/j.atmosenv.2012.12.009, 2013.

Lim, S., Lee, M., and Yoo, H. J.: Size distributions, mixing state, and morphology of refractory black carbon in an urban atmosphere of northeast Asia during summer, Science of the Total Environment, 856, https://doi.org/10.1016/j.scitotenv.2022.158436, 2023.

Linke, C., Ibrahim, I., Schleicher, N., Hitzenberger, R., Andreae, M. O., Leisner, T., and Schnaiter, M.: A novel single-cavity three-wavelength photoacoustic spectrometer for atmospheric aerosol research, Atmos. Meas. Tech., 9, 5331–5346, https://doi.org/10.5194/amt-9-5331-2016, 2016.

Liu, D., Allan, J. D., Young, D. E., Coe, H., Beddows, D., Fleming, Z. L., Flynn, M. J., Gallagher, M. W., Harrison, R. M., Lee, J., Prevot, A. S. H., Taylor, J. W., Yin, J., Williams, P. I., and Zotter, P.: Size distribution, mixing state and source apportionment of black carbon aerosol in London during winter time, Atmos Chem Phys, 14, 10061–10084, https://doi.org/10.5194/acp-14-10061-2014, 2014.

Liu, D., Flynn, M., Gysel, M., Targino, A., Crawford, I., Bower, K., Choularton, T., Jurnyi, Z., Steinbacher, M., Hglin, C., Curtius, J., Kampus, M., Petzold, A., Weingartner, E., Baltensperger, U., and Coe, H.: Single particle

Formatted: Font: (Default) Times New Roman, 10 pt, Font color: Auto

Formatted: English (United Kingdom)

Formatted: Font: (Default) Times New Roman, 10 pt, Font color: Auto

Formatted: Font: (Default) Times New Roman, 10 pt, Font color: Auto

Formatted: Font: (Default) Times New Roman, 10 pt, Font color: Auto

Formatted: Font: (Default) Times New Roman, 10 pt, Font color: Auto

characterization of black carbon aerosols at a tropospheric alpine site in Switzerland, Atmos. Chem. Phys., 10, 7389–7407, https://doi.org/10.5194/acp-10-7389-2010, 2010.

Liu, D., Quennehen, B., Darbyshire, E., Allan, J. D., Williams, P. I., Taylor, J. W., J.-B. Bauguitte, S., Flynn, M. J., Lowe, D., Gallagher, M. W., Bower, K. N., Choularton, T. W., and Coe, H.: The importance of Asia as a source of black carbon to the European Arctic during springtime 2013, Atmos Chem Phys, 15, 11537–11555, https://doi.org/10.5194/acp-15-11537-2015, 2015.

Liu, D., Joshi, R., Wang, J., Yu, C., Allan, J. D., Coe, H., Flynn, M. J., Xie, C., Lee, J., Squires, F., Kotthaus, S., Grimmond, S., Ge, X., Sun, Y., and Fu, P.: Contrasting physical properties of black carbon in urban Beijing between winter and summer, Atmos Chem Phys, 19, 6749–6769, https://doi.org/10.5194/acp-19-6749-2019, 2019.

Liu, H., Pan, X., Liu, D., Liu, X., Chen, X., Tian, Y., Sun, Y., Fu, P., and Wang, Z.: Mixing characteristics of refractory black carbon aerosols at an urban site in Beijing, Atmos. Chem. Phys., 20, 5771–5785, https://doi.org/10.5194/acp-20-5771-2020, 2020.

Liu, J., Fan, S., Horowitz, L. W., and Levy, H.: Evaluation of factors controlling long-range transport of black carbon to the Arctic, Journal of Geophysical Research Atmospheres, 116, https://doi.org/10.1029/2010JD015145, 2011.

Liu, S., Aiken, A. C., Gorkowski, K., Dubey, M. K., Cappa, C. D., Williams, L. R., Herndon, S. C., Massoli, P., Fortner, E. C., Chhabra, P. S., Brooks, W. A., Onasch, T. B., Jayne, J. T., Worsnop, D. R., China, S., Sharma, N., Mazzoleni, C., Xu, L., Ng, N. L., Liu, D., Allan, J. D., Lee, J. D., Fleming, Z. L., Mohr, C., Zotter, P., Szidat, S., and Prévôt, A. S. H.: Enhanced light absorption by mixed source black and brown carbon particles in UK winter, Nat. Commun., 6, https://doi.org/10.1038/ncomms9435, 2015.

Ludwig, V., Spreen, G., and Pedersen, L. T.: Evaluation of a new merged sea-ice concentration dataset at 1 km resolution from thermal infrared and passive microwave satellite data in the arctic, Remote Sens, 12, 1–28, https://doi.org/10.3390/rs12193183, 2020.

Ma, Y., Huang, C., Jabbour, H., Zheng, Z., Wang, Y., Jiang, Y., Zhu, W., Ge, X., Collier, S., and Zheng, J.: Mixing state and light absorption enhancement of black carbon aerosols in summertime Nanjing, China, Atmos. Environ., 222, https://doi.org/10.1016/j.atmosenv.2019.117141, 2020.

Matsui, H.: Black carbon simulations using a size- and mixing-state-resolved three-dimensional model: 1. Radiative effects and their uncertainties, J Geophys Res, 121, 1793–1807, https://doi.org/10.1002/2015JD023998, 2016.

McMeeking, G. R., Hamburger, T., Liu, D., Flynn, M., Morgan, W. T., Northway, M., Highwood, E. J., Krejci, R., Allan, J. D., Minikin, A., and Coe, H.: Black carbon measurements in the boundary layer over western and northern Europe, Atmos Chem Phys, 10, 9393–9414, https://doi.org/10.5194/acp-10-9393-2010, 2010.

Mortin, J., Svensson, G., Graversen, R. G., Kapsch, M. L., Stroeve, J. C., and Boisvert, L. N.: Melt onset over Arctic sea ice controlled by atmospheric moisture transport, Geophys Res Lett, 43, 6636–6642, https://doi.org/10.1002/2016GL069330, 2016.

Moteki, N., Kondo, Y., and Nakamura, S. ichi: Method to measure refractive indices of small nonspherical particles: Application to black carbon particles, J Aerosol Sci, 41, 513–521, https://doi.org/10.1016/j.jaerosci.2010.02.013, 2010.

Moteki, N. and Kondo, Y.: Dependence of laser-induced incandescence on physical properties of black carbon aerosols: Measurements and theoretical interpretation, Aerosol Science and Technology, 44, 663–675, https://doi.org/10.1080/02786826.2010.484450, 2010.

Moteki, N., Kondo, Y., Oshima, N., Takegawa, N., Koike, M., Kita, K., Matsui, H., and Kajino, M.: Size dependence of wet removal of black carbon aerosols during transport from the boundary layer to the free troposphere, Geophys Res Lett, 39, https://doi.org/10.1029/2012GL052034, 2012.

Formatted: Font: (Default) Times New Roman, 10 pt, Font color: Auto

Formatted: Font: (Default) Times New Roman, 10 pt, Font color: Auto

Formatted: Font: (Default) Times New Roman, 10 pt, Font color: Auto

Moteki, N., Ohata, S., Yoshida, A., and Adachi, K.: Constraining the complex refractive index of black carbon particles using the complex forward-scattering amplitude, Aerosol Science and Technology, 57, 678–699, https://doi.org/10.1080/02786826.2023.2202243, 2023.

Motos, G., Schmale, J., Corbin, J. C., Zanatta, M., Baltensperger, U., and Gysel-Beer, M.: Droplet activation behaviour of atmospheric black carbon particles in fog as a function of their size and mixing state, Atmos Chem Phys, 19, 2183–2207, https://doi.org/10.5194/acp-19-2183-2019, 2019a.

Motos, G., Schmale, J., Corbin, J. C., Modini, R. L., Karlen, N., Bertò, M., Baltensperger, U., and Gysel-Beer, M.: Cloud droplet activation properties and scavenged fraction of black carbon in liquid-phase clouds at the high-alpine research station Jungfraujoch (3580ma.s.l.), Atmos Chem Phys, 19, 3833–3855, https://doi.org/10.5194/acp-19-3833-2019, 2019b.

Motos, G., Corbin, J. C., Schmale, J., Modini, R. L., Bertò, M., Kupiszewski, P., Baltensperger, U., and Gysel-Beer, M.: Black Carbon Aerosols in the Lower Free Troposphere are Heavily Coated in Summer but Largely Uncoated in Winter at Jungfraujoch in the Swiss Alps, Geophys Res Lett, 47, https://doi.org/10.1029/2020GL088011, 2020.

Muller, K., Lehmann, S., Van Pinxteren, D., Gnauk, T., Niedermeier, N., Wiedensohler, A., and Herrmann, H.: Atmospheric Chemistry and Physics Particle characterization at the Cape Verde atmospheric observatory during the 2007 RHaMBLe intensive, Atmos. Chem. Phys, 2709–2721 pp., 2010.

Müller, T., Laborde, M., Kassell, G., and Wiedensohler, A.: Design and performance of a three-wavelength LED-based total scatter and backscatter integrating nephelometer, Atmos Meas Tech, 4, 1291–1303, https://doi.org/10.5194/amt-4-1291-2011, 2011.

Nithin, B., Kompalli, S. K., and Babu, S. S.: Black carbon mixing state and light-absorption enhancement under different air mass regimes over a tropical coastal site, Atmos. Res., 331, https://doi.org/10.1016/j.atmosres.2025.108641, 2026.

Nenes, A., Conant, W. C., and Seinfeld, J. H.: Black carbon radiative heating effects on cloud microphysics and implications for the aerosol indirect effect 2. Cloud microphysics, Journal of Geophysical Research: Atmospheres, 107, https://doi.org/10.1029/2002jd002101, 2002.

Pandolfi, M., Alados-Arboledas, L., Alastuey, A., Andrade, M., Angelov, C., Artiñano, B., Backman, J., Baltensperger, U., Bonasoni, P., Bukowiecki, N., Collaud Coen, M., Conil, S., Coz, E., Crenn, V., Dudoitis, V., Ealo, M., Eleftheriadis, K., Favez, O., Fetfatzis, P., Fiebig, M., Flentje, H., Ginot, P., Gysel, M., Henzing, B., Hoffer, A., Holubova Smejkalova, A., Kalapov, I., Kalivitis, N., Kouvarakis, G., Kristensson, A., Kulmala, M., Lihavainen, H., Lunder, C., Luoma, K., Lyamani, H., Marinoni, A., Mihalopoulos, N., Moerman, M., Nicolas, J., O'Dowd, C., Petäjä, T., Petit, J. E., Marc Pichon, J., Prokopciuk, N., Putaud, J. P., Rodríguez, S., Sciare, J., Sellegri, K., Swietlicki, E., Titos, G., Tuch, T., Tunved, P., Ulevicius, V., Vaishya, A., Vana, M., Virkkula, A., Vratolis, S., Weingartner, E., Wiedensohler, A., and Laj, P.: A European aerosol phenomenology - 6: Scattering properties of atmospheric aerosol particles from 28 ACTRIS sites, Atmos Chem Phys, 18, 7877–7911, https://doi.org/10.5194/acp-18-7877-2018, 2018.

Pan, X., Zhang, Y., Xue, C., Kuhn, U., Hrabe de Angelis, I., Pöhlker, C., Ditas, J., Heins, L., Aardema, H. M., Slagter, H. A., Calleja, M. Ll., Dragoneas, A., Walter, D., Nillius, B., Wang, Q., Ma, N., Su, H., Pöschl, U., Haug, G. H., Schiebel, R., and Cheng, Y.: Black Carbon in the Marine Atmosphere: Concentration and Mixing State From Coastal to Remote Atlantic Regions, Journal of Geophysical Research: Atmospheres, 131, https://doi.org/10.1029/2025JD045346, 2026.

Park, J., Dall'osto, M., Park, K., Gim, Y., Jin Kang, H., Jang, E., Park, K. T., Park, M., Soo Yum, S., Jung, J., Yong Lee, B., and Jun Yoon, Y.: Shipborne observations reveal contrasting Arctic marine, Arctic terrestrial and Pacific marine aerosol properties, Atmos Chem Phys, 20, 5573–5590, https://doi.org/10.5194/acp-20-5573-2020, 2020.

Pernov, J. B., Beddows, D., Thomas, D. C., Dall´Osto, M., Harrison, R. M., Schmale, J., Skov, H., and Massling, A.: Increased aerosol concentrations in the High Arctic attributable to changing atmospheric transport patterns, NPJ Clim Atmos Sci, 5, https://doi.org/10.1038/s41612-022-00286-y, 2022.

Formatted: Font: (Default) Times New Roman, 10 pt, Font color: Auto

Formatted: Font: (Default) Times New Roman, 10 pt, Font color: Auto

Petzold, A. and Schönlinner, M.: Multi-angle absorption photometry - A new method for the measurement of aerosol light absorption and atmospheric black carbon, J Aerosol Sci, 35, 421–441, https://doi.org/10.1016/j.jaerosci.2003.09.005, 2004.

Popovicheva, O. B., Evangeliou, N., Eleftheriadis, K., Kalogridis, A. C., Sitnikov, N., Eckhardt, S., and Stohl, A.: Black Carbon Sources Constrained by Observations in the Russian High Arctic, Environ Sci Technol, 51, 3871–3879, https://doi.org/10.1021/acs.est.6b05832, 2017.

Quinn, P. K., Miller, T. L., Bates, T. S., Ogren, J. A., Andrews, E., and Shaw, G. E.: A 3-year record of simultaneously measured aerosol chemical and optical properties at Barrow, Alaska, Journal of Geophysical Research: Atmospheres, 107, https://doi.org/10.1029/2001jd001248, 2002.

Quinn, P. K., Bates, T. S., Baum, E., Doubleday, N., Fiore, A. M., Flanner, M., Fridlind, A., Garrett, T. J., Koch, D., Menon, S., Shindell, D., Stohl, A., and Warren, S. G.: Short-lived pollutants in the Arctic: their climate impact and possible mitigation strategies, Atmos. Chem. Phys, 1723–1735 pp., 2008.

Raatikainen, T., Brus, D., Hyvärinen, A. P., Svensson, J., Asmi, E., and Lihavainen, H.: Black carbon concentrations and mixing state in the Finnish Arctic, Atmos Chem Phys, 15, 10057–10070, https://doi.org/10.5194/acp-15-10057-2015, 2015.

Raatikainen, T., Brus, D., Hooda, R. K., Hyvarinen, A. P., Asmi, E., Sharma, V. P., Arola, A., and Lihavainen, H.: Size-selected black carbon mass distributions and mixing state in polluted and clean environments of northern India, Atmos. Chem. Phys., 17, 371–383, https://doi.org/10.5194/acp-17-371-2017, 2017.

Rantanen, M., Karpechko, A. Y., Lipponen, A., Nordling, K., Hyvärinen, O., Ruosteenoja, K., Vihma, T., and Laaksonen, A.: The Arctic has warmed nearly four times faster than the globe since 1979, Commun Earth Environ, 3, https://doi.org/10.1038/s43247-022-00498-3, 2022.

Romshoo, B., Patil, J., Michels, T., Müller, T., Kloft, M., and Pöhlker, M.: Improving the predictions of black carbon (BC) optical properties at various aging stages using a machine-learning-based approach, Atmos. Chem. Phys., 24, 8821–8846, https://doi.org/10.5194/acp-24-8821-2024, 2024.

Rose, T., Crewell, S., Löhnert, U., and Simmer, C.: A network suitable microwave radiometer for operational monitoring of the cloudy atmosphere, Atmos Res, 75, 183–200, https://doi.org/10.1016/j.atmosres.2004.12.005, 2005.

Sand, M., Berntsen, T. K., Seland, Ø., and Kristjánsson, J. E.: Arctic surface temperature change to emissions of black carbon within Arctic or midlatitudes, Journal of Geophysical Research Atmospheres, 118, 7788–7798, https://doi.org/10.1002/jgrd.50613, 2013.

Schmale, J., Arnold, S. R., Law, K. S., Thorp, T., Anenberg, S., Simpson, W. R., Mao, J., and Pratt, K. A.: Local Arctic Air Pollution: A Neglected but Serious Problem, Earths Future, 6, 1385–1412, https://doi.org/10.1029/2018EF000952, 2018.

Schmale, J., Zieger, P., and Ekman, A. M. L.: Aerosols in current and future Arctic climate, Nat Clim Chang, 11, 95–105, https://doi.org/10.1038/s41558-020-00969-5, 2021.

Schmale, J., Sharma, S., Decesari, S., Pernov, J., Massling, A., Hansson, H. C., Von Salzen, K., Skov, H., Andrews, E., Quinn, P. K., Upchurch, L. M., Eleftheriadis, K., Traversi, R., Gilardoni, S., Mazzola, M., Laing, J., and Hopke, P.: Pan-Arctic seasonal cycles and long-term trends of aerosol properties from 10 observatories, Atmos Chem Phys, 22, 3067–3096, https://doi.org/10.5194/acp-22-3067-2022, 2022.

Schmeisser, L., Backman, J., Ogren, J. A., Andrews, E., Asmi, E., Starkweather, S., Uttal, T., Fiebig, M., Sharma, S., Eleftheriadis, K., Vratolis, S., Bergin, M., Tunved, P., and Jefferson, A.: Seasonality of aerosol optical properties in the Arctic, Atmos Chem Phys, 18, 11599–11622, https://doi.org/10.5194/acp-18-11599-2018, 2018.

Schnaiter, M., Linke, C., Möhler, O., Naumann, K. H., Saathoff, H., Wagner, R., Schurath, U., and Wehner, B.: Absorption amplification of black carbon internally mixed with secondary organic aerosol, Journal of Geophysical Research D: Atmospheres, 110, 1–11, https://doi.org/10.1029/2005JD006046, 2005.

Formatted: Font: (Default) Times New Roman, 10 pt, Font color: Auto

Formatted: Font: (Default) Times New Roman, 10 pt, Font color: Auto

Schulz, H., Zanatta, M., Bozem, H., Richard Leaitch, W., Herber, A. B., Burkart, J., Willis, M. D., Kunkel, D., Hoor, P. M., Abbatt, J. P. D., and Gerdes, R.: High Arctic aircraft measurements characterising black carbon vertical variability in spring and summer, Atmos Chem Phys, 19, 2361–2384, https://doi.org/10.5194/acp-19-2361-2019, 2019.

Schwarz, J. P., Gao, R. S., Spackman, J. R., Watts, L. A., Thomson, D. S., Fahey, D. W., Ryerson, T. B., Peischl, J., Holloway, J. S., Trainer, M., Frost, G. J., Baynard, T., Lack, D. A., de Gouw, J. A., Warneke, C., and Del Negro, L. A.: Measurement of the mixing state, mass, and optical size of individual black carbon particles in urban and biomass burning emissions, Geophys Res Lett, 35, https://doi.org/10.1029/2008GL033968, 2008.

Seinfeld, J. H., & Pandis, S. N, Atmospheric chemistry and physics: From air pollution to climate change. John Wiley & Sons, Inc., 2006.

Sharma, S., Andrews, E., Barrie, L. A., Ogren, J. A., and Lavoué, D.: Variations and sources of the equivalent black carbon in the high Arctic revealed by long-term observations at Alert and Barrow: 1989-2003, Journal of Geophysical Research Atmospheres, 111, https://doi.org/10.1029/2005JD006581, 2006.

Sharma, S., Richard Leaitch, W., Huang, L., Veber, D., Kolonjari, F., Zhang, W., Hanna, S. J., Bertram, A. K., and Ogren, J. A.: An evaluation of three methods for measuring black carbon in Alert, Canada, Atmos. Chem. Phys., 17, 15225–15243, https://doi.org/10.5194/acp-17-15225-2017, 2017.

Shiraiwa, M., Kondo, Y., Moteki, N., Takegawa, N., Miyazaki, Y., and Blake, D. R.: Evolution of mixing state of black carbon in polluted air from Tokyo, Geophys Res Lett, 34, https://doi.org/10.1029/2007GL029819, 2007.

Shiraiwa, M., Kondo, Y., Moteki, N., Takegawa, N., Sahu, L. K., Takami, A., Hatakeyama, S., Yonemura, S., and Blake, D. R.: Radiative impact of mixing state of black carbon aerosol in Asian outflow, Journal of Geophysical Research Atmospheres, 113, https://doi.org/10.1029/2008JD010546, 2008.

Shiraiwa, M., Kondo, Y., Iwamoto, T., and Kita, K.: Amplification of light absorption of black carbon by organic coating, Aerosol Science and Technology, 44, 46–54, https://doi.org/10.1080/02786820903357686, 2010.

Spreen, G., Kaleschke, L., and Heygster, G.: Sea ice remote sensing using AMSR-E 89-GHz channels, J Geophys Res Oceans, 113, https://doi.org/10.1029/2005JC003384, 2008.

Stein, A. F., Draxler, R. R., Rolph, G. D., Stunder, B. J. B., Cohen, M. D., and Ngan, F.: Noaa's hysplit atmospheric transport and dispersion modeling system, https://doi.org/10.1175/BAMS-D-14-00110.1, 1 December 2015.

Stohl, A.: Characteristics of atmospheric transport into the Arctic troposphere, Journal of Geophysical Research Atmospheres, 111, https://doi.org/10.1029/2005JD006888, 2006.

Stohl, A., Klimont, Z., Eckhardt, S., Kupiainen, K., Shevchenko, V. P., Kopeikin, V. M., and Novigatsky, A. N.: Black carbon in the Arctic: The underestimated role of gas flaring and residential combustion emissions, Atmos Chem Phys, 13, 8833–8855, https://doi.org/10.5194/acp-13-8833-2013, 2013.

Taketani, F., Miyakawa, T., Takashima, H., Komazaki, Y., Pan, X., Kanaya, Y., and Inoue, J.: Shipborne observations of atmospheric black carbon aerosol particles over the Arctic Ocean, Bering Sea, and North Pacific Ocean during september 2014, J Geophys Res, 121, 1914–1921, https://doi.org/10.1002/2015JD023648, 2016.

Taylor, J. W., Allan, J. D., Allen, G., Coe, H., Williams, P. I., Flynn, M. J., Le Breton, M., Muller, J. B. A., Percival, C. J., Oram, D., Forster, G., Lee, J. D., Rickard, A. R., Parrington, M., and Palmer, P. I.: Size-dependent wet removal of black carbon in Canadian biomass burning plumes, Atmos Chem Phys, 14, 13755–13771, https://doi.org/10.5194/acp-14-13755-2014, 2014.

Thackeray, C. W. and Hall, A.: An emergent constraint on future Arctic sea-ice albedo feedback, Nat Clim Change, 9, 972–978, https://doi.org/10.1038/s41558-019-0619-1, 2019.

Thakur, R. C., Arun, B. S., Gogoi, M. M., Thamban, M., Thayyen, R. J., Redkar, B. L., and Suresh Babu, S.: Multi-layer distribution of Black Carbon and inorganic ions in the snowpacks of western Himalayas and snow albedo forcing, Atmos. Environ., 261, https://doi.org/10.1016/j.atmosenv.2021.118564, 2021.

Formatted: Font: (Default) Times New Roman, 10 pt, Font color: Auto

Formatted: Font: (Default) Times New Roman, 10 pt, Font color: Auto

Formatted: Font: (Default) Times New Roman, 10 pt, Font color: Auto

Tinorua, S., Denjean, C., Nabat, P., Bourrianne, T., Pont, V., Gheusi, F., and Leclerc, E.: Higher absorption enhancement of black carbon in summer shown by 2-year measurements at the high-altitude mountain site of Pic du Midi Observatory in the French Pyrenees, Atmos. Chem. Phys., 24, 1801–1824, https://doi.org/10.5194/acp-24-1801-2024, 2024.

Tomasi, C., Vitale, V., Lupi, A., Di Carmine, C., Campanelli, M., Herber, A., Treffeisen, R., Stone, R. S., Andrews, E., Sharma, S., Radionov, V., von Hoyningen-Huene, W., Stebel, K., Hansen, G. H., Myhre, C. L., Wehrli, C., Aaltonen, V., Lihavainen, H., Virkkula, A., Hillamo, R., Ström, J., Toledano, C., Cachorro, V. E., Ortiz, P., de Frutos, A. M., Blindheim, S., Frioud, M., Gausa, M., Zielinski, T., Petelski, T., and Yamanouchi, T.: Aerosols in polar regions: A historical overview based on optical depth and in situ observations, https://doi.org/10.1029/2007JD008432, 27 August 2007.

Tunved, P., Ström, J., and Krejci, R.: Arctic aerosol life cycle: Linking aerosol size distributions observed between 2000 and 2010 with air mass transport and precipitation at Zeppelin station, Ny-Ålesund, Svalbard, Atmos Chem Phys, 13, 3643–3660, https://doi.org/10.5194/acp-13-3643-2013, 2013.

Ueda, S., Nakayama, T., Taketani, F., Adachi, K., Matsuki, A., Iwamoto, Y., Sadanaga, Y., and Matsumi, Y.: Light absorption and morphological properties of soot-containing aerosols observed at an East Asian outflow site, Noto Peninsula, Japan, Atmos. Chem. Phys., 16, 2525–2541, https://doi.org/10.5194/acp-16-2525-2016, 2016.

Walbröl, A., Crewell, S., Engelmann, R., Orlandi, E., Griesche, H., Radenz, M., Hofer, J., Althausen, D., Maturilli, M., and Ebell, K.: Atmospheric temperature, water vapour and liquid water path from two microwave radiometers during MOSAiC, Sci Data, 9, https://doi.org/10.1038/s41597-022-01504-1, 2022.

Wang, Q., Cao, J., Han, Y., Tian, J., Zhu, C., Zhang, Y., Zhang, N., Shen, Z., Ni, H., Zhao, S., and Wu, J.: Sources and physicochemical characteristics of black carbon aerosol from the southeastern Tibetan Plateau: Internal mixing enhances light absorption, Atmos. Chem. Phys., 18, 4639–4656, https://doi.org/10.5194/acp-18-4639-2018, 2018.

Wang, Q. Y., Huang, R. J., Cao, J. J., Tie, X. X., Ni, H. Y., Zhou, Y. Q., Han, Y. M., Hu, T. F., Zhu, C. S., Feng, T., Li, N., and Li, J. D.: Black carbon aerosol in winter northeastern Qinghai-Tibetan Plateau, China: The source, mixing state and optical property, Atmos. Chem. Phys., 15, 13059–13069, https://doi.org/10.5194/acp-15-13059-2015, 2015.

Wang, Y., Li, W., Huang, J., Liu, L., Pang, Y., He, C., Liu, F., Liu, D., Bi, L., Zhang, X., and Shi, Z.: Nonlinear Enhancement of Radiative Absorption by Black Carbon in Response to Particle Mixing Structure, Geophys. Res. Lett., 48, https://doi.org/10.1029/2021GL096437, 2021.

Wendisch, M., Brückner, M., Crewell, S., Ehrlich, A., Notholt, J., Lüpkes, C., Macke, A., Burrows, J. P., Rinke, A., Quaas, J., Maturilli, M., Schemann, V., Shupe, M. D., Akansu, E. F., et al.: Atmospheric and Surface Processes, and Feedback Mechanisms Determining Arctic Amplification, Bull Am Meteorol Soc, 104, E208–E242, https://doi.org/10.1175/BAMS-D-21-0218.1, 2023.

Winiger, P., Andersson, A., Eckhardt, S., Stohl, A., Semiletov, I. P., Dudarev, O. V., Charkin, A., Shakhova, N., Klimont, Z., Heyes, C., and Gustafsson, Ö.: Siberian Arctic black carbon sources constrained by model and observation, Proc Natl Acad Sci U S A, 114, E1054–E1061, https://doi.org/10.1073/pnas.1613401114, 2017.

Woods, C. and Caballero, R.: The role of moist intrusions in winter arctic warming and sea ice decline, J Clim, 29, 4473–4485, https://doi.org/10.1175/JCLI-D-15-0773.1, 2016.

Wu, C., Wu, D., and Zhen Yu, J.: Quantifying black carbon light absorption enhancement with a novel statistical approach, Atmos. Chem. Phys., 18, 289–309, https://doi.org/10.5194/acp-18-289-2018, 2018.

Wu, Y., Cheng, T., Liu, D., Allan, J. D., Zheng, L., and Chen, H.: Light Absorption Enhancement of Black Carbon Aerosol Constrained by Particle Morphology, Environ. Sci. Technol., 52, 6912–6919, https://doi.org/10.1021/acs.est.8b00636, 2018.

Yang, Y., Müller, T., Poulain, L., Atabakhsh, S., Holanda, B. A., Voigtländer, J., Arora, S., and Pöhlker, M. L.: Microphysical properties of refractory black carbon aerosols for different air masses at a central European background site, Atmos Chem Phys, 25, 8637–8655, https://doi.org/10.5194/acp-25-8637-2025, 2025.

Formatted: Font: (Default) Times New Roman, 10 pt, Font color: Auto

Yang, Y. (2024). Assessing Absorption Enhancement in Black Carbon: Insights into Mixing State Heterogeneity. Zenodo. https://doi.org/10.5281/zenodo.17312995.

Zanatta, M., Gysel, M., Bukowiecki, N., Müller, T., Weingartner, E., Areskoug, H., Fiebig, M., Yttri, K. E., Mihalopoulos, N., Kouvarakis, G., Beddows, D., Harrison, R. M., Cavalli, F., Putaud, J. P., Spindler, G., Wiedensohler, A., Alastuey, A., Pandolfi, M., Sellegri, K., Swietlicki, E., Jaffrezo, J. L., Baltensperger, U., and Laj, P.: A European aerosol phenomenology-5: Climatology of black carbon optical properties at 9 regional background sites across Europe, Atmos. Environ., 145, 346–364, https://doi.org/10.1016/j.atmosenv.2016.09.035, 2016.

Zanatta, M., Laj, P., Gysel, M., Baltensperger, U., Vratolis, S., Eleftheriadis, K., Kondo, Y., Dubuisson, P., Winiarek, V., Kazadzis, S., Tunved, P., and Jacobi, H. W.: Effects of mixing state on optical and radiative properties of black carbon in the European Arctic, Atmos Chem Phys, 18, 14037–14057, https://doi.org/10.5194/acp-18-14037-2018, 2018.

Zanatta, M., Mertes, S., Jourdan, O., Dupuy, R., Järvinen, E., Schnaiter, M., Eppers, O., Schneider, J., Jurányi, Z., and Herber, A.: Airborne investigation of black carbon interaction with low-level, persistent, mixed-phase clouds in the Arctic summer, Atmos Chem Phys, 23, 7955–7973, https://doi.org/10.5194/acp-23-7955-2023, 2023.

Zeng, L., Tan, T., Zhao, G., Du, Z., Hu, S., Shang, D., and Hu, M.: Overestimation of black carbon light absorption due to mixing state heterogeneity, NPJ Clim Atmos Sci, 7, https://doi.org/10.1038/s41612-023-00535-8, 2024.

Zhai, J., Yang, X., Li, L., Bai, B., Liu, P., Huang, Y., Fu, T. M., Zhu, L., Zeng, Z., Tao, S., Lu, X., Ye, X., Wang, X., Wang, L., and Chen, J.: Absorption Enhancement of Black Carbon Aerosols Constrained by Mixing-State Heterogeneity, Environ Sci Technol, 56, 1586–1593, https://doi.org/10.1021/acs.est.1c06180, 2022.

Zhang, Y., Cheng, X., Liu, J., and Hui, F.: The potential of sea ice leads as a predictor for summer Arctic sea ice extent, Cryosphere, 12, 3747–3757, https://doi.org/10.5194/tc-12-3747-2018, 2018.

Zhang, Y., Favez, O., Canonaco, F., Liu, D., Močnik, G., Amodeo, T., Sciare, J., Prévôt, A. S. H., Gros, V., and Albinet, A.: Evidence of major secondary organic aerosol contribution to lensing effect black carbon absorption enhancement, NPJ Clim Atmos Sci, 1, https://doi.org/10.1038/s41612-018-0056-2, 2018.

Zhang, Y., Su, H., Kecorius, S., Ma, N., Wang, Z., Sun, Y., Zhang, Q., Pöschl, U., Wiedensohler, A., Andreae, M. O., and Cheng, Y.: Extremely low-volatility organic coating leads to underestimation of black carbon climate impact, One Earth, 6, 158–166, https://doi.org/10.1016/j.oneear.2023.01.009, 2023.

Zhang, Z., Wang, J., Riemer, N., Liu, C., Wang, J., Jin, Y., Tian, Z., Chen, G., Wang, B., Huang, X., Ding, A., and Wang, S.: Inversion Approach for Inferring Mixing State and Improving Optical Estimation of Coated Black Carbon Using Bulk-Volume Variables and Number-Size Distributions, Environ. Sci. Technol., 60, 3998–4007, https://doi.org/10.1021/acs.est.5c10094, 2026.

Zhao, C. and Garrett, T. J.: Effects of Arctic haze on surface cloud radiative forcing, Geophys Res Lett, 42, 557–564, https://doi.org/10.1002/2014GL062015, 2015.

Zieger, P., Heslin-Rees, D., Karlsson, L., Koike, M., Modini, R., and Krejci, R.: Black carbon scavenging by low-level Arctic clouds, Nat Commun, 14, https://doi.org/10.1038/s41467-023-41221-w, 2023.

Formatted: Font: (Default) Times New Roman, 10 pt

Formatted: Font: (Default) Times New Roman, 10 pt, Font color: Auto

Formatted: Font: (Default) Times New Roman, 10 pt, Font color: Auto

Formatted: Font: (Default) Times New Roman, 10 pt, Font color: Auto